Flying Qualities Analysis and Piloted Simulation Testing of a Lift+Cruise Vehicle with Propulsion Failures in Hover and Low-Speed Conditions

George Altamirano
Aerospace Engineer

Justin Matt
Aerospace Engineer
Flight Dynamics Branch
NASA Langley Research Center
Hampton, VA, USA

John Foster
Aerospace Engineer

Peter Suh
Aerospace Engineer

Curtis Hanson
Aerospace Engineer
Flight Controls and Dynamics Branch
NASA Armstrong Flight Research Center
Edwards, CA, USA

Carlos Malpica
Aerospace Engineer
Aeromechanics Branch

Stefan Schuet
Computer Engineer
Intelligent Systems Division
NASA Ames Research Center
Moffett Field, CA, USA

ABSTRACT

The recent emergence of electric-Vertical Take-Off and Landing (eVTOL) vehicles for Urban Air Mobility (UAM) applications has resulted in a wide variety of configurations with unique stability and control characteristics. NASA is currently conducting research to develop conceptual design tools to accelerate public acceptance of these vehicles which includes requirements for safety during failure scenarios. This paper summarizes progress toward a toolbox for predicting flying qualities of eVTOL vehicles during critical propulsion failures that could impact the allowable design of the vehicle geometry or control system. Key topics include unique vulnerabilities of eVTOL/multirotor vehicles to propulsion failures, relevant flying qualities design metrics, and simulation modeling requirements for assessing flying qualities degradation due to failures. Results of a piloted simulation study conducted in the NASA Ames Vertical Motion Simulator (VMS) are presented. The VMS experiment was designed to assess and validate key handling qualities and safety design metrics for propulsion failures. These results show the correlation between control system design requirements and the degradation in handling qualities for various propulsion failures.

NOTATION

Symbols

B_m	Dynamic friction coefficient
C_x, C_y, C_z	Body-axis nondimensional aerodynamic force coefficients
C_l, C_m, C_n	Body-axis nondimensional aerodynamic moment coefficients
C_T	Rotor thrust coefficient
C_{M_x}, C_{M_y}	Roll and pitch coefficient at rotor hub
i_c	Motor current command (A)
i_m	Motor current (A)
L	Derivative matrix for inflow
M	Mass matrix for inflow
n_g	Gear ratio
n_p	Number of pole pairs
p, q, r	Body-axis roll, pitch, and yaw rates (rad/s or deg/s)
Q	Rotor torque (N $\cdot$ m or ft $\cdot$ lb)
Q_{h_0}	Nominal hover rotor torque (N $\cdot$ m or ft $\cdot$ lb)
q_{hub}, p_{hub}	Pitch and roll rates in rotor hub coordinate frame (rad/s or deg/s)
R	Rotor radius (ft)
R_s	Stator resistance (Ohms)
r	Radial position of blade-element (ft)
T_{DN}	Drivetrain control allocation matrix
u, v, w	Body-axis translational velocity components (ft/s)
u_a	Aircraft control input vector (i.e., motor torques)
V_{h_0}	Nominal hover stator voltage (V)
V_s	Stator voltage (V)
x	Full-order aircraft state vector
x_c	Vector of state commands
x_R	Reduced-order aircraft state vector
α	Angle of attack (rad or deg)
β	Sideslip angle (rad or deg)
β_{rot}	Blade flapping angle (rad or deg)
β_0	Coning angle (rad or deg)
β_{1c}, β_{1s}	Longitudinal, lateral flapping angle (rad or deg)
$\Delta\phi_4$	Roll angle perturbation four seconds after a step input (rad or deg)
$\Delta\phi_{pk}$	Maximum roll angle perturbation (rad or deg)

$\Delta\theta_4$	Pitch angle perturbation four seconds after a step input (rad or deg)
$\Delta\theta_{pk}$	Maximum pitch angle perturbation (rad or deg)
Δt	Time step (s)
δ	Pilot inceptor input vector
δ_{lat}	Pilot lateral input
δ_{lon}	Pilot longitudinal input
δ_{max}	Maximum control deflection
δ_{min}	Minimum control deflection
δ_{ped}	Pilot pedal input
δ_{thr}	Pilot throttle input
λ_v	Flux linkage (V/rad/s)
λ	Inflow ratio
λ_0	Uniform inflow ratio
$\lambda_{1c}, \lambda_{1s}$	Longitudinal, lateral inflow perturbation
ϕ, θ, ψ	Euler roll, pitch, and yaw angles (rad or deg)
ψ_{az}	Rotor azimuth angle (rad or deg)
τ_c	Motor torque command (N · m or ft · lb)
τ_m	Motor torque (N · m or ft · lb)
τ_p	Phase delay (s)
ω_c	Crossover frequency (rad/s)
ω_{BW}	Small-amplitude response bandwidth (rad/s)
Ω	Rotor speed (rad/s)
ζ	ACAH damping parameters

Acronyms

AAM	Advanced Air Mobility
ACAH	Attitude Command/Attitude Hold
BEMT	Blade-Element Momentum Theory
DEP	Distributed Electric Propulsion
DRB	Disturbance Rejection Bandwidth
DRP	Disturbance Rejection Peak
eVTOL	electric-Vertical Take-Off and Landing
FCS	Flight Control System
GM	Gain margin
HQR	Handling Qualities Rating
HQTE	Handling Qualities Task Element
MTE	Mission Task Element
NAS	National Airspace System
OLOP	Open-Loop Onset Point
PM	Phase margin
PIO	Pilot-Induced Oscillation
PMSM	Permanent Magnet Synchronous Motor
RCDH	Rate Command/Direction Hold
RCHH	Rate Command/Height Hold
RHSS	Right Hand Side Stick
ROC	Rate of Climb
SOC	State of Charge
TCL	Thrust Control Lever
TRC	Translational Rate Command
UAM	Urban Air Mobility
VMS	Vertical Motion Simulator
VTOL	Vertical Take-Off and Landing

Superscripts

^{T}	transpose
*	term with saturation limits applied
$\dot{}$	first derivative with respect to time
$\ddot{}$	second derivative with respect to time

INTRODUCTION

Advancements in electric motor and battery technologies have increased the potential for distributed electric propulsion (DEP) systems to support electric-Vertical Take-Off and Landing (eVTOL) rotorcraft designs. The development and integration of eVTOL vehicles into the National Airspace System (NAS) has raised questions related to flying qualities and safety, including: 1) Are existing flight mechanics design tools adequate for these new designs? and 2) How will these new designs fare in the presence of propulsion failures? The rapid and iterative design cycles observed in industry suggest a need for refinement of rotorcraft design tools. One area identified by NASA as a technical gap is the need for new handling qualities analysis tools at the conceptual design level (Ref. 1). This framework is being extended to support the design and analysis of rotorcraft under failure conditions, considering the Operational and Safe Flight Envelopes.

Development of these tools requires comparison against higher-fidelity models and validation of predicted handling qualities using piloted assessments. Previous NASA research (Ref. 2) described simulation-based studies to develop modeling requirements and identify preliminary metrics that are necessary to ensure flight safety in the event of propulsion failures. These results identified potential critical flying qualities metrics that enable a reliable assessment of safety necessary to inform changes in the vehicle or control system design.

A piloted simulation test was completed in the NASA Ames Vertical Motion Simulator (VMS) to assess proposed flying qualities and safety metrics. A flight dynamics model of a NASA designed lift+cruise concept vehicle was developed and integrated with an electric powertrain model with failure modes. Several hover and low-speed tasks were evaluated using Mission Task Elements (MTE) from ADS-33E-PRF (Ref. 3) and Handling Qualities Task Elements (HQTE) under evaluation by the FAA (currently in development) for eVTOL vehicles (Refs. 4 and 5). This paper presents preliminary results from the piloted simulation study that includes handling qualities analysis of propulsion failures and recommendations for critical metrics that define minimum levels of safety.

The paper is structured as follows. The next section presents a review of relevant literature involving flying qualities of VTOL configurations and studies involving failures of rotorcraft. This is followed by a description of the lift+cruise flight dynamics model used for piloted simulation including the vehicle parameters, modeling methods, control system, and failure mode implementation. A safety assessment is then presented to show the impact of failures on critical metrics involving motor torque saturation, pilot-induced oscillations (PIO), and interaxis coupling. The experimental setup is then outlined including descriptions of the facility, pilot inceptor configurations, evaluation tasks, and test procedure. The piloted simulation results are highlighted for each maneuver

followed by a summary of key findings and next steps for this research.

PRIOR PUBLICATION

The rapid development of modern eVTOL aircraft with numerous control effectors and highly augmented control modes has raised new questions regarding piloted handling qualities. The unique vulnerabilities of these aircraft to propulsion failures create a demand for thorough analysis of flying qualities requirements during degraded flight. Historically, research is sparse on this topic for hovering vehicles; however, previous work on handling qualities during failures laid the foundation for the approach and test methodology used in the current research.

A pilot failure rating scale was originally proposed in 1988 and evaluated using a piloted simulation of single-axis hardover failures in the UH-60 at the NASA Ames VMS (Ref. 6), and later tested in flight (Ref. 7). This research was the principal work in establishing the "transients following failures" criteria in ADS-33E-PRF. Later, in the early 2000s, piloted simulation tests of the V-22 Osprey were conducted to evaluate flying qualities following failure (Refs. 8-10). MTEs were evaluated for both the failed and unfailed aircraft using the Cooper-Harper scale, and failure transients were additionally evaluated using a modified version of the failure recovery scale from Ref. 7. These works provided key insights for handling qualities evaluations in the presence of failures, including recommendations for failure transient assessment and usage of the Cooper-Harper scale during upset, and serve as the first example of handling quality assessment during failures for modern VTOL aircraft.

Several recent works have discussed flying qualities as defined in ADS-33E-PRF and proposed ADS-33F-PRF (Ref. 11) for preliminary eVTOL concepts (Refs. 12-16). The first piloted simulation of an eVTOL aircraft at the NASA Ames Vertical Motion Simulation (VMS) was recently conducted for a six-passenger quadrotor concept vehicle design (Refs. 17-18). Configurations were designed to either Level 1 or Level 2 flying qualities based on several specifications, and handling qualities were evaluated for MTEs as defined by ADS-33E-PRF and for custom MTEs designed for UAM vehicles. Initial results showed that designed Level 1 flying qualities did not readily translate to Level 1 handling qualities assessment. Additionally, degradations in control system responses were not significantly reflected by piloted assessments during testing of all MTEs. Specifically, almost no change in Cooper-Harper ratings were seen for the precision hover maneuver, while the lateral and vertical maneuvers showed small degradations.

Similar piloted simulation tests have been carried out at other institutions. Jones and Jusko (Ref. 19) evaluated handling qualities of a quadrotor concept vehicle in a fixed-base simulator at the German Aerospace Center (DLR). Newly proposed flight test maneuvers (FTMs) for eVTOL vehicles that are scalable based on vehicle geometry were used for evaluation. Similarly, Wechner et al. (Ref. 20) evaluated handling qualities for a lift+cruise configuration eVTOL

vehicle using a piloted virtual reality simulation. MTEs from the European Organisation for Civil Aviation Equipment (EUROCAE), originally adapted from ADS-33E, and MTEs designed by the authors specifically for UAM vehicles were evaluated. Single motor failures were injected during MTEs. Failures were found to have negligible impact on handling qualities in the hover regime, as the effects were mitigated by the TRC-style control system.

FLIGHT DYNAMICS MODEL

Vehicle Description

A NASA designed lift+cruise concept vehicle (Refs. 21 and 22) was the baseline configuration for this research. A rendering of the vehicle is shown in Fig. 1 and its design is representative of several distributed electric VTOL aircraft in development for UAM and advanced air mobility (AAM) operations (Refs. 23-24). The primary aircraft and rotor properties that were used for simulation development are given in Table 1.

Figure 1. Rendering of lift+cruise reference design.

Table 1. Lift+cruise configuration data.

Aircraft Data	
Vehicle mass	202.6 slug
Wingspan	47.7 ft
Mean chord	3.94 ft
Wing area	231 ft^2
Roll moment of inertia	6,480 slug $\cdot$ ft^2
Pitch moment of inertia	4,500 slug $\cdot$ ft^2
Yaw moment of inertia	9,611 slug $\cdot$ ft^2
Rotor Data	
Number of rotors	8
Blades per rotor	2
Rotor radius	5 ft
Rotor inertia	13.49 slug $\cdot$ ft^2
Blade twist	-0.227 rad
Blade pitch at 75% radius	0.279 rad
Chord taper ratio	0.75
Root chord	1.23 ft

The configuration blends a fixed-wing airframe with eight variable-RPM lifting rotors. The airframe uses a high wing design to provide additional wing tip clearance for lateral reposition tasks in low-speed maneuvering. The design of the lifting rotors was driven by disk loading with a hard constraint on maximum diameter of 10 feet to mitigate the effects of

large rotor inertia on rotor speed bandwidth. The inboard motors are canted outward to increase the achievable control power in the yaw axis for directional control in near hover conditions. All lifting rotors are fixed-pitch, hingeless, and two-bladed to simplify the mechanisms required for alignment with the flow in forward flight. Each rotor has a dedicated electric motor that is connected to a single gearbox. Adjacent rotors rotate in opposite directions to cancel out lateral-directional moments and gyroscopic effects when the rotor states are symmetric. The front rotors were placed below the booms to reduce their adverse impact on the wing and aft rotors during transition.

The stability and control characteristics change significantly among hover, transition, and forward flight phases. As such, different control strategies are required based on the mode of operation. In hover and low speed conditions, the lifting rotors are the primary source of lift and the main control effectors for stability augmentation. The hover flight control system (FCS) bandwidth is driven by the rotor speed response characteristics, rotor inertia, available power from the electric motors, and structural limitations. In forward flight, it operates like conventional fixed wing aircraft using trailing edge surfaces for control and a pusher propeller for propulsion. In this flight mode, the main wing is the primary source of lift, and the lifting rotors are aligned with the flow to minimize drag contributions.

Aerodynamic and Propulsion Models

Rotor performance was modeled using blade-element momentum theory (BEMT) with blade flapping, inflow, and rotor speed dynamics. This approach discretizes the blade geometry into span-wise segments and evaluates the section aerodynamic characteristics at radial stations located at the center of each segment. The forces and moments were integrated with respect to the blade radius (R) and averaged over the rotor azimuth (ψ_{az}). The section characteristics were evaluated using four span-wise segments and eight azimuth locations per rotation.

The rotors experience edgewise flow components during longitudinal and lateral translations. This causes asymmetric blade section characteristics that are important to model because they cause significant hub-frame roll and pitch moments that affect rotor trim states and power consumption. The wake induced velocities at the rotor disk were represented using a Pitt-Peters inflow model (Ref. 25). The inflow model has states representing a uniform component (λ_0) and longitudinal/lateral perturbations (λ_c, λ_s). L and M are the derivative and mass matrices based on potential flow theory solutions and the mass of an impermeable disk in translation (Ref. 26). The loading variables are the thrust coefficient (C_T), rotor roll moment coefficient (C_{M_x}) and pitch moment coefficient (C_{M_y}). The last term includes angular rate effects at the rotor hub which includes terms for the pitch/roll rate at the rotor hub (q_{hub}, p_{hub}), first derivative of longitudinal/lateral blade flapping components ($\dot{\beta}_{1c}, \dot{\beta}_{1s}$), and a matrix with the wake curvature factor (A).

$$LM \begin{bmatrix} \dot{\lambda}_0 \\ \dot{\lambda}_c \\ \dot{\lambda}_s \end{bmatrix} + \begin{bmatrix} \lambda_0 \\ \lambda_c \\ \lambda_s \end{bmatrix} = L \begin{bmatrix} C_T \\ -C_{M_y} \\ C_{M_x} \end{bmatrix} + A \begin{bmatrix} q_{hub} - \dot{\beta}_{1c} \\ p_{hub} - \dot{\beta}_{1s} \end{bmatrix} \quad (1)$$

The wake-induced downwash varies with radial location and azimuth as shown in Eq. 2.

$$\lambda = \lambda_0 + (r/R)(\lambda_c \cos \psi_{az} + \lambda_s \sin \psi_{az}) \quad (2)$$

The blade flapping angle and its derivative in the rotating coordinate frame are given in Eqs. 3-4 as a function of the longitudinal (β_{1c}) and lateral (β_{1s}) components.

$$\beta_{rot} = \beta_{1c} \cos \psi_{az} + \beta_{1s} \sin \psi_{az} \quad (3)$$

$$\dot{\beta}_{rot} = -\Omega\beta_{1c} \sin \psi_{az} + \Omega\beta_{1s} \cos \psi_{az} \quad (4)$$

The rate of change of the lateral ($\dot{\beta}_{1s}$) and longitudinal ($\dot{\beta}_{1c}$) flapping angles influence the inflow dynamics and are defined in Eqs. 5-6 using the constraint $\dot{\beta}_{1c} \cos(\psi_{az}) + \dot{\beta}_{1s} \sin(\psi_{az}) = 0$ (Ref. 26).

$$\dot{\beta}_{1s} = (\frac{\ddot{\beta}_{rot}}{\Omega} + \Omega\beta_{rot}) \cos \psi_{az} \quad (5)$$

$$\dot{\beta}_{1c} = -(\frac{\ddot{\beta}_{rot}}{\Omega} + \Omega\beta_{rot}) \sin \psi_{az} \quad (6)$$

The airframe was modeled from computational fluid dynamics (CFD) data. Aerodynamic force and moment coefficients were computed over a grid of elevation and azimuth angles for relative wind, shown in Fig. 2. These data were implemented as a linearly interpolated lookup table. Force and moment coefficients are plotted against traditional airflow angles in Fig. 3. Longitudinal and lateral-directional forces and moments were made symmetric and anti-symmetric about the x-axis, respectively.

Although the airframe aerodynamic forces and moments would be small for hover conditions, the contributions could be significant during some maneuvers or crosswind conditions. A significant change in static pitch stability with relative wind angle is shown in Fig. 3, where the pitching moment is stabilizing at low sideslip angles but destabilizing at large sideslip angles, which could be experienced during sideward or backward flight. Roll and yaw static stability varies between stable and unstable depending on the sideslip angle. For example, directional stability is positive at 0 deg sideslip angle but nearly neutral at 90 deg sideslip.
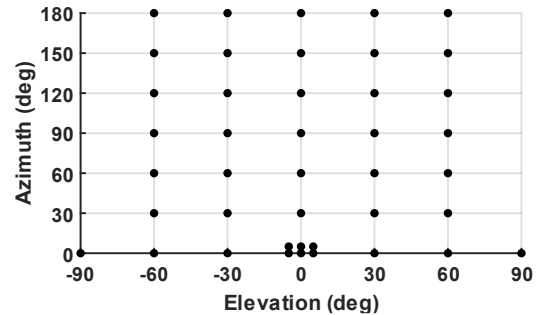
Figure 2. Airframe CFD test points.
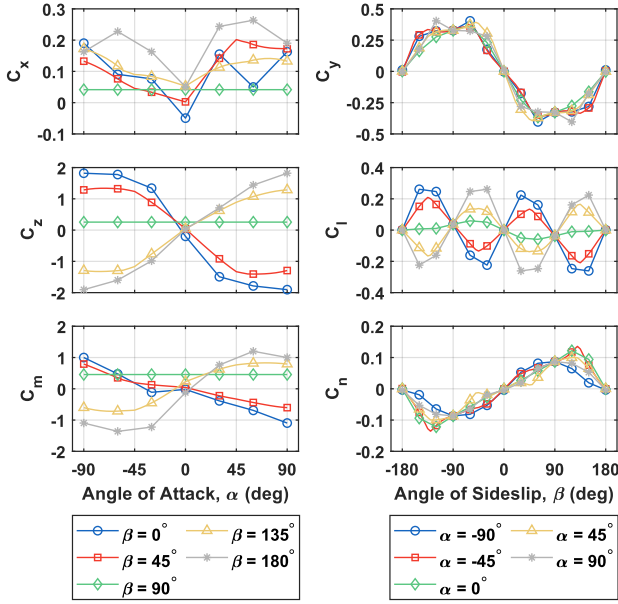
Figure 3. Airframe longitudinal (left) and lateral-directional (right) force and moment coefficients.

Aerodynamic interactions between rotors and airframe surfaces were not modeled. These interactions can be significant and may cause unsteady aerodynamic effects that are important to capture. Increasing the model fidelity is an ongoing area of research.

Powertrain Model

Powertrain models were developed to translate flight controller torque commands (τ_c) into motor shaft torques (τ_m). A simple and complex version of the powertrain was derived to examine different levels of model fidelity. The complex powertrain consists of a single permanent magnet synchronous motor (PMSM) with water-glycol thermal cooling, a 3-phase space vector pulse width modulation inverter, a motor controller employing field-oriented control and flux weakening control, and an air-cooled battery pack. No cross-shafting is assumed, and fault modeling was not accommodated in the complex powertrain. The complex powertrain details are not reviewed here, but source material used for its development is provided in Refs. 27-32.

The simple powertrain approximates the performance of the complex powertrain performance within the rated envelope of the PMSM under nominal test conditions. Several key assumptions can be made to simplify the complex powertrain such as: 1) constant battery voltage; 2) current command equating to current; 3) a fixed PMSM stator winding temperature; and 4) the direct (D) axis of the PMSM nonlinear equations of motion is removed. With these simplifications, the governing dynamics of the powertrain simplify to effects of torque, dynamic friction, and rotor inertia. The simple powertrain retains limits used in the complex powertrain on torque command, current command rate, and voltage limitations arising from inverter saturation protection. The

motor torque is converted by gearing into motor shaft torque and applied to each rotor with no-cross-shafting.

Both simple and complex powertrains shared the same sizing coefficients. The powertrain coefficients were sized beginning with the NASA Design and Analysis of Rotorcraft (NDARC) (Ref. 33) specification on maximum continuous power for each motor and battery energy capacity. Flexibility was allowed in the allocation of rated continuous torque and motor rated continuous speed. The motors were sized to maximize rated speed, instead of rated torque after initial testing to avoid hitting voltage limits during fault scenarios. The battery packs were sized for the RVLT reference mission such that the end-of-mission state of charge (SOC) provide a minimum loaded bus voltage of 600V; therefore, the loaded battery voltage at full charge was approximately 700V. Table 2 presents the sizing parameters and powertrain constants relevant to the simple powertrain; the sizing parameters are also closely approximated by those in the complex powertrain. For the VMS tests, the simple powertrain was used during evaluation tasks. The simple powertrain output torque could be directly set to a constant torque value during a single or dual motor failure scenario.

Table 2. Battery and electric motor sizing parameters and powertrain constants.

Parameter	Value
Max Continuous Power	91.7 kW
Rated Continuous Torque	98.2 Nm
Peak Torque	196.5 Nm
Stator Current Limit	440.3 A_{pk}
Current Rate Limit	3.36 $\frac{kA_{pk}}{s}$
Battery Voltage (100% SOC)	700 V
Stator Voltage Limit	350 V_{pk}
Design Speed	8.9 kRPM
Gear Ratio	7.616
Rated Winding Temperature	130 °C
Battery Energy Capacity	1,215 MJ
Max Battery C-Rating	3
Back EMF Constant	0.2976 $\frac{V}{rad/s}$
Rated Winding Resistance	0.0195 Ohm
Inductance – Direct (D) Axis	0.225 mH
Inductance – Quadrature (Q) Axis	0.225 mH
Flux Linkage	0.049 $\frac{V}{rad/s}$
Pole Pairs	6

5

The simple powertrain equations are reviewed here. The flight control system provides reference motor torque commands (τ_c) that are input to the powertrain model. This is first converted to a reference current command (i_c) as shown in Eq. 7 as a function of the number of pole pairs (n_p) and flux linkage (λ_v). Saturation and rate limits are then applied to the reference current. The current with limits applied is designated as i_c^*.

$$i_c = \frac{\tau_c}{\left(\frac{3}{2}\right) n_p \lambda_v} \qquad (7)$$

The Q-axis stator voltage (V_s) is defined in Eq. 8 as a function of the stator resistance (R_s), gear ratio (n_g), number of poles, rotor speed (Ω), and flux linkage. The second term in Eq. 8 is typically referred to as the back-EMF.

$$V_s = i_c^* R_s + n_g \Omega n_p \lambda_v \qquad (8)$$

Voltage saturation is applied using the stator voltage limit listed in Table 2 to obtain V_s^*. This voltage limit was derived from the effect of flux weakening control used for inverter saturation protection on corresponding complex motors.

Assuming that the voltage limit is applied, the voltage-limited motor current (i_m^*) can be recovered. The stator Q-axis voltage equation in Eq. 8 is rearranged to solve for the voltage limited current as shown in Eq. 9. In place of the traditional stator Q axis voltage, is the limited commanded stator Q-axis voltage (V_s^*). The voltage limited current is then converted to motor torque subject to upstream current and voltage limitations as shown in Eq. 10.

$$i_m^* = \frac{V_s^* - n_g \Omega n_p \lambda_v}{R_s} \qquad (9)$$

$$\tau_m = \frac{3}{2} i_m^* n_p \lambda_v - n_g \Omega B_m \qquad (10)$$

Notably, Eq. 9 assumes that the back-EMF has not been weakened; this condition places more restriction on the current with the simple powertrain than on the complex powertrain with flux weakening control. Operations of the simple powertrain past its rated speed and torque conditions will result in quicker torque degradation than would be nominally present in the complex powertrain. Eq. 10 assumes only the importance of dynamic friction (B_m) but not that of static friction, which is a good approximation at high motor speeds. Insertion of motor torque failures can be conducted by setting τ_m in Eq. 11 equal to a pre-determined torque setting. Further details about motor failure implementation are provided in a later section.

The rotor angular acceleration ($\dot{\Omega}$) is computed by taking the difference of shaft motor torque and aerodynamic load (Q) from the blades, and then dividing by the total shaft inertia (J_{zz}). The rotor speed can then be computed by integration.

$$\dot{\Omega} = \frac{n_g \tau_m - Q}{J_{zz}} \qquad (11)$$

Flight Control System

A flight control system for hover and low speed conditions was developed to enable the response types listed in Table 3. Attitude Command/Attitude Hold (ACAH) and Translational Rate Command (TRC) response-types were implemented in the roll/lateral and pitch/longitudinal axes. The yaw and the heave response types were Rate Command/Direction Hold (RCDH) and Rate Command/Height Hold (RCHH), respectively.

Table 3. Control response types.

Axis	Response-Type
Roll, lateral	ACAH, TRC
Pitch, longitudinal	ACAH, TRC
Yaw	RCDH
Heave	RCHH

A top-level simulation diagram is shown in Fig. 4. Command models were used to generate state commands (x_c) from pilot control inputs (δ). The feedback controller generates reference motor torque commands (τ_c) that are input to the powertrain model. The nonlinear aircraft model receives the rotor speeds (Ω) output from the powertrain model to compute the rotor and aircraft states.
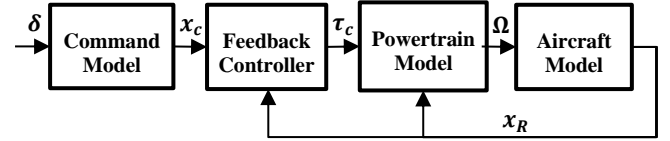
Figure 4. Top-level simulation diagram.

The full-order state vector, shown in Eq. 12, consists of Euler angles (ϕ, θ, ψ), body velocities (u, v, w), body-axis angular rates (p, q, r), rotor rotational speed (Ω_k), lateral/longitudinal blade flapping components ($\beta_{1c_k}, \beta_{1s_k}$), and inflow components ($\lambda_{0_k}, \lambda_{1c_k}, \lambda_{1s_k}$). The index term ($k$) ranges from one to eight.

$$x^T = [\phi, \theta, \psi, u, v, w, p, q, r,$$
$$\Omega_k, \beta_{1c_k}, \beta_{1s_k}, \lambda_{0_k}, \lambda_{1c_k}, \lambda_{1s_k}] \text{ for } k = 1,2,\dots 8 \ (12)$$

The hover control input, $u_a = \left[\tau_{c_k}\right]$ for $k = 1,2,\dots 8$, is a vector of the motor torque commands. Inputs for the pusher propeller and trailing edge control surfaces were neglected since the conditions studied were in hover/low speed without transition phases. The pilot inceptor inputs (δ) were mapped to individual motor torque commands using a control allocation matrix (T_{DN}) as shown in Eq. 13. The pilot inceptor inputs consist of lateral (δ_{lat}), longitudinal (δ_{lon}), pedal (δ_{ped}), and throttle (δ_{thr}) channels. The components of the control allocation matrix are provided in Table 4.

$$u_a = T_{DN} * \delta \qquad (13)$$

Table 4. Control allocation matrix (T_{DN}).

Motor Number	δ_{lat}	δ_{lon}	δ_{ped}	δ_{thr}
1	6	6	24	-10
2	6	6	-24	-10
3	-6	6	24	-10
4	-6	6	-24	-10
5	6	-6	-24	-10
6	6	-6	24	-10
7	-6	-6	-24	-10
8	-6	-6	24	-10

A reduced order linear model was used for control design. The states of the reduced order model (x_R) consist of the rigid-body six degree of freedom states and rotor speed states (Eq. 14). The reduced order model was obtained by using the *modred()* function in MATLAB®.

$$x_R^T = [\phi, \theta, \psi, u, v, w, p, q, r, \Omega_k] \text{ for } k = 1,2, \dots 8 \text{ (14)}$$

A linear quadratic integral (LQI) feedback control system with integral action applied to the roll, pitch, yaw, and heave axes was used for command tracking and feedback stabilization. The LQI feedback gains were tuned to attain Level 1 disturbance rejection bandwidth (DRB) and disturbance rejection peak (DRP) responses per proposed ADS-33F-PRF standards. The DRB and DRP for each axis and control mode are shown in Table 5.

The relative stability margins from the broken-loop frequency responses were assessed to ensure minimum phase and gain margins of 45 degrees and 6 dB and are shown in Table 6. The margins were computed using loop breaks in the feedback system for individual variables ϕ, θ, ψ, and w. Reference excitation signals were used to generate the feedback/error frequency responses. It is important to note that loop breaks at different locations should also be considered to reveal potentially lower margins, such as at the actuator signals, plant output, and using other feedback variables; however, these locations were not analyzed in the presented control law development and analysis.

Second order linear filters were used as command models for the pitch and roll axes, and first order linear filters were used as command models for the yaw and heave axes. Table 7 lists the second and first order command model parameters. The command model parameters were tuned per ADS-33E-PRF small-amplitude attitude criteria for the pitch, roll and yaw axes. A proportional-integral controller was wrapped around the ACAH controller to enable TRC modes. The translational and vertical velocity bandwidths were tuned using proposed criteria in Refs. 34 and 35. Figure 5 presents the roll and pitch ACAH bandwidth/phase delay responses. Figures 6 and 7 present the translational rate and heave bandwidth/phase delay responses, respectively.

Table 5. Disturbance rejection metrics.

Axis	DRB (rad/s)	DRP (dB)
Roll	0.97	2.45
Pitch	0.78	1.99
Yaw	1.04	2.46
Heave	1.26	2.04

Table 6. Stability margins and crossover frequency.

Axis	GM (dB)	PM (deg)	ω_c (rad/s)
Roll	12.3	53	3.7
Pitch	10.4	49	4.1
Yaw	20.2	56	3.1
Heave	19.3	66	1.6

Table 7. Command model parameters.

Order	Axis	ω_n (rad/s)	ζ	τ_n (s)
Second	Roll	2.5	1	N/A
Second	Pitch	2.5	1	N/A
First	Surge	N/A	N/A	10
First	Sway	N/A	N/A	10
First	Yaw	N/A	N/A	1
First	Heave	N/A	N/A	0.75
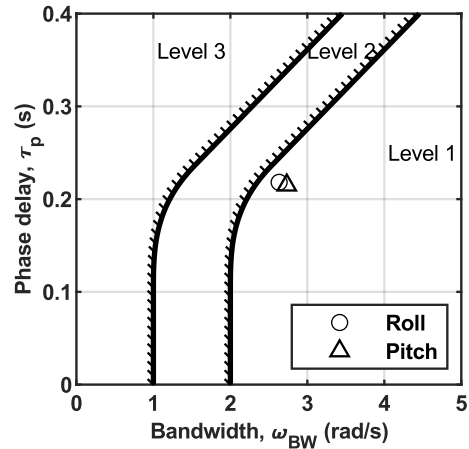
Figure 5. ADS-33E small-amplitude attitude response criteria.
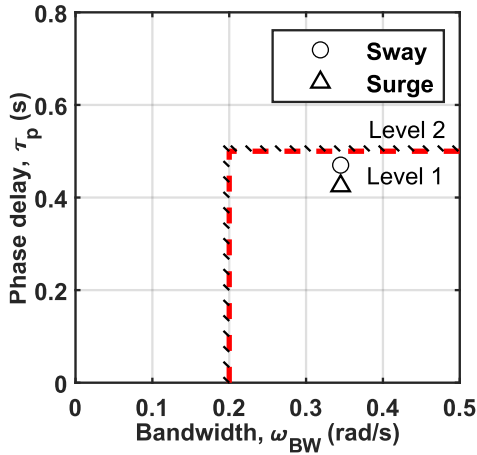
Figure 6. TRC bandwidth response criteria.
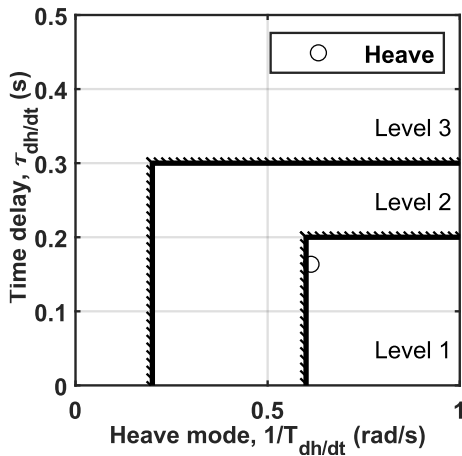
Figure 7. Heave bandwidth response criteria.

Failure Mode Implementation

Two failure scenarios were implemented based on Failure Modes Effects and Criticality (FMECA) studies of eVTOL vehicles (Ref. 36).

- Single motor failure applied to motor 1
- Low torque failure simultaneously applied to motors 3 and 4

Switches in the powertrain model were used to initiate the failures at a specified simulation time where the motor torque applied to the rotor shaft instantly changes to a predetermined value when the failure switch is triggered. In the case of the single motor failure, the torque applied to the shaft of the failed motor instantaneously changes to zero. As a result, the corresponding rotor speed and the thrust decay to zero. In the case of the dual low torque failure, the motor torque applied to the rotor shaft instantly changes to 60% of its nominal hover value and is frozen at that setting for the remainder of that simulation run. This represents a partial loss of torque and simultaneous frozen throttle command for motors 3 and 4.

Example time histories of the single zero torque failure and the dual low torque failure are shown in Fig. 8. In these examples, the vehicle is initialized in a hover and the failure is triggered at time=10 seconds. For the single motor failure, the torque applied to the rotor shaft instantly goes to zero, and the rotor thrust decays as the rotor speed approaches zero. Motor 1 was selected for the single motor failure case because it is an outboard motor with the maximum roll moment arm and in a failed state it causes asymmetries in rotor states that could lead to control system and handling qualities degradation. Once the rotor speed reaches zero, it is considered stopped and does not rotate further. For the dual low torque case, the output motor torque was set to 60% of the hover torque and held at that command for the remainder of the simulation run. Motors 3 and 4 were selected for the dual low torque failure because they are adjacent motors and cause asymmetries in trim rotor states. Autorotation and windmilling effects were not modeled.

(a) Single motor failure (single fail)

(b) Dual low torque failure (dual fail)
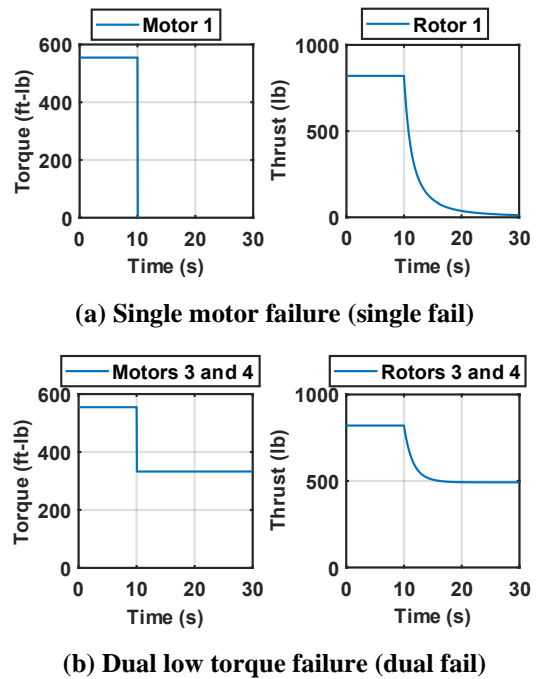
Figure 8. Example time histories of applied rotor shaft torque (Q) and rotor thrust for each failure scenario.

SAFETY ASSESSMENT

Many eVTOL concept vehicles rely on variable-RPM motors for lift and control augmentation in hover and transition phases. This poses unique safety challenges because the effects of electric motor bandwidth and saturation on stability and control system performance have not been extensively studied, particularly in the presence of one or more propulsion failures. Simulation analysis was conducted to evaluate the impact of propulsion failures on 1) trim conditions in a failed state, 2) susceptibility to pilot-induced oscillations (PIO) due to motor torque saturation, and 3) interaxis coupling between roll, pitch, and heave axes. The purpose of this analysis was to demonstrate methods and application of existing metrics to assess the impact of propulsion failures and to inform the piloted simulation test discussed in a later section. It is important to note that this analysis was largely dependent on

the closed-loop feedback gains, command model parameters, control allocation approach, and simulation model fidelity. Implementation of fault detection systems, failure accommodating control logic, or alternative control system methodologies could improve controller performance in the presence of propulsion failures or other off-nominal conditions; however, was not included in this study.

Trim Conditions in Failed State

The aircraft was trimmed in a hover with the single motor failure and the dual low torque failure using the nominal control allocation matrix listed in Table **4** and nominal feedback gains. In both failure scenarios, some of the non-failed motors trim at conditions with reduced control margins to compensate for the body-axis moments introduced from complete or partial loss of rotor thrust. Table 8 presents the trim stator voltages (V_s) and rotor shaft torque (Q) as a ratio of the nominal hover voltage (V_{h_0}) and required torque (Q_{h_0}).

In a single motor failure, the trim motor torque and voltages are highest for motor 2 because it is compensating for the roll and pitch moments introduced by the loss of thrust of rotor 1. Motor 6 also has a notable increase in stator voltage and torque to compensate for the roll moment due to loss of thrust for rotor 1.

In a dual low torque failure, motor 1 has the highest trim motor voltage and torque requirements. This is likely to compensate for the nose-down pitch moment introduced by the decrease in thrust for rotors 3 and 4. There is a notable increase in voltage and torque for motor 8 and decreases in torque requirements for motor 5.

Table 8. Hover trim motor torque and voltages for single motor no torque and dual low torque failures.

Motor Number	Single Fail		Dual Fail	
	V_s/V_{h_0}	Q/Q_{h_0}	V_s/V_{h_0}	Q/Q_{h_0}
1	0	0	1.28	1.62
2	1.31	1.69	1.09	1.18
3	1.13	1.27	0.77	0.60
4	0.99	0.99	0.77	0.60
5	1.10	1.21	0.64	0.42
6	1.23	1.50	0.92	0.86
7	0.71	0.51	1.06	1.13
8	0.89	0.80	1.26	1.57

Motor Torque Requirements

The decrease in control margin for some of the motors due to propulsion failures increases the likelihood of saturation with pilot inputs and external disturbances. Motor saturation can lead to FCS instabilities, PIO susceptibility, and significant inter-axis coupling. Duda (Ref. 37) proposed the Open-Loop Onset Point (OLOP) criteria to predict category II PIOs within the pilot-vehicle system. This process requires determination

of the frequency at which actuator rate limiters are activated for the first time using maximum control input magnitudes. These are referred to as the open-loop onset frequencies (ω_{OLOP}). The OLOP boundaries are defined using a Nichols chart which characterize PIO prone regions using the frequency response obtained from breaking the loop at the rate limiter, and then evaluating the phase and magnitude at the open-loop onset frequencies. This method was originally developed for fixed-wing aircraft and has been recently applied to rotorcraft in Ref. 38 with extensions to include a sophisticated pilot model and task-specific control input magnitudes.

The OLOP criterion was applied in this paper to assess PIO susceptibility due to motor torque saturation. The closed-loop motor torque requirements were determined using simulated pilot frequency sweeps for baseline (no failure), single no torque failure, and dual low torque failure scenarios. The vehicle was trimmed at hover at the start of the frequency sweep and the motor voltage and torque limits were bypassed to evaluate the closed-loop torque requirements. Figure 9 shows the torque-to-pilot input frequency responses for the worst-case motor (motor 2 for single fail and motor 1 for dual fail) for the roll, pitch, and heave axes in ACAH. Analysis of the yaw axis was omitted. The onset frequencies are marked at 25%, 50%, 75%, and 100% of the maximum pilot inceptor control deflection. The maximum control input magnitudes were 20 deg for roll/pitch and 15 ft/s for heave. If there is no marker, then saturation was not reached for that control input magnitude. The trim motor torque was subtracted from the time history of each motor to center the mean around zero prior to spectral analysis and effectively evaluate the torque perturbation from trim. It should be noted that the torque response to lateral and longitudinal inputs is nonlinear due to the height-hold active in the controller, as a torque increase is required for both positive and negative roll or pitch motions to maintain altitude. Analysis of the measured frequency responses showed that the linear portion of the response is dominant at frequencies above approximately 1.5 rad/s for all input magnitudes studied. Nonetheless, it is important to note that this nonlinear response could lead to earlier torque saturation than predicted.

Figure 9(a) shows that the baseline onset frequency for the roll axis occurs at approximately 4.6 rad/s for 100% maximum lateral control deflection. In contrast, the single and dual motor failures result in torque saturation at approximately 1.75 rad/s and 2 rad/s for 100% lateral control deflection. respectively. The single failure case shows motor torque saturation for 25% control deflection at approximately 3.8 rad/s, which is less than the baseline onset frequency for 100% amplitude. Figure 9(b) shows that the baseline configuration results in motor torque saturation for 100% and 75% of maximum longitudinal deflection at approximately 4 and 5 rad/s, respectively. The presence of failures significantly reduces the onset frequency corresponding to 100% deflection. For both failure scenarios, the onset frequency for 50% control deflection occurs before the corresponding baseline 100% onset frequency. Heave inputs

result in higher motor torque requirements in comparison to the other axes for majority of the frequency range of interest. In both failure scenarios, the onset frequency at 25% control deflection is equal to or less than the corresponding baseline onset frequency for 100% control deflection.
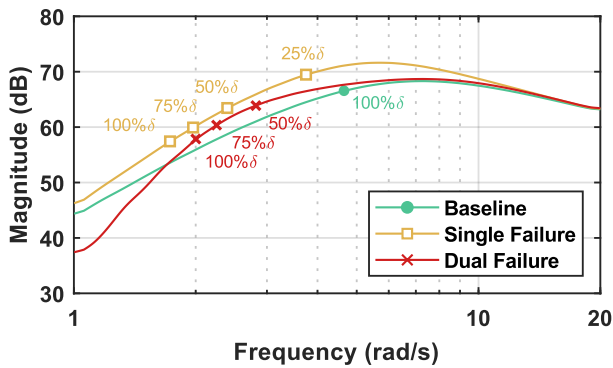
(a) τ/δ_{lat} (Nm/rad)
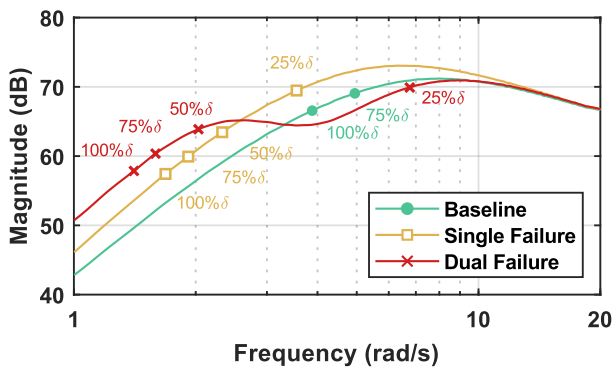
(b) τ/δ_{lon} (Nm/rad)
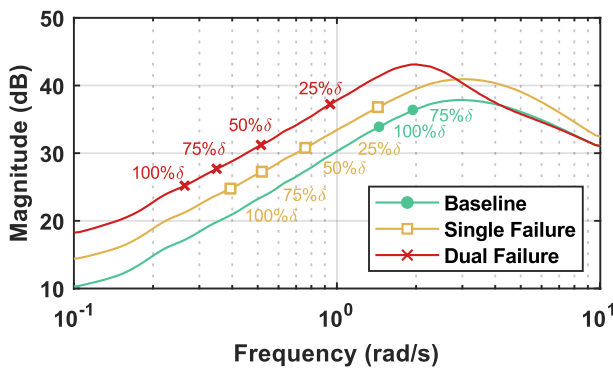
(c) τ/δ_{thr} (Nm/ft/s)

Figure 9. Motor torque frequency responses in ACAH.

Figure 10 shows the OLOP criteria applied to the roll, pitch, and heave axes using the onset frequencies identified in Fig. 9. The magnitude and phase points were computed using the frequency response with the loop broken at the error signal. This approach was used to separate the effects of torque saturation on OLOP criteria for each axis, as is done for decoupled FCS. Further analysis of open-loop responses with the loop broken at different locations, such as at the input

to the torque limiter should be considered. These boundaries were originally proposed for fixed-wing vehicles and have not been validated or extensively studied for eVTOL rotorcraft. Pilot models were not included in this analysis.
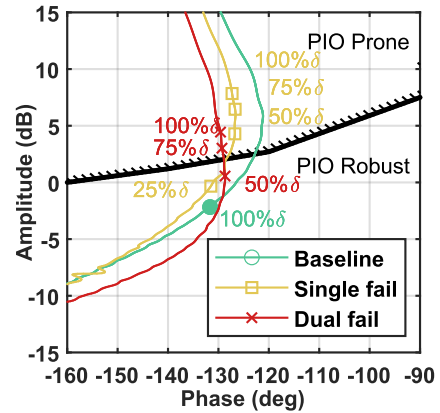
(a) lateral
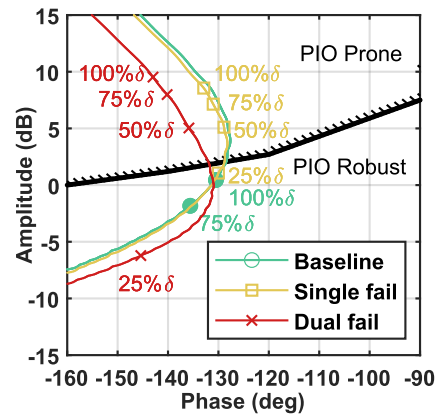
(b) longitudinal
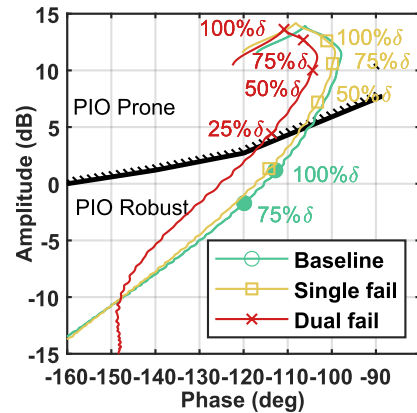
(c) heave

Figure 10. OLOP criteria in ACAH.

The OLOP results for the baseline (no failure) configuration indicate the vehicle is PIO robust for 100% control input magnitudes. The presence of propulsion failures results in degradations into PIO prone regions. For example, the onset frequencies for control deflections greater than 50% of the

maximum control input magnitude result in degradations into the PIO prone region for the longitudinal and heave axes. Overall, this criterion indicates a clear degradation in OLOP criteria due to propulsion failures and suggests that the vehicle is PIO prone for control amplitudes well within the normal operating range of a pilot.

Roll and Pitch Due to Heave

Among the primary effects of motor saturation are degraded stability margins and off-axis responses that are not commanded by the pilot. As shown in Figure 9(c), heave inputs can result in saturation at a wide range of operational pilot input frequencies, even for 25% and 50% control deflections. Currently, however, ADS-33E-PRF does not specify any quantitative requirements for the roll or pitch response due to heave inputs in hover and low-speed flight. As such, to characterize this critical coupling response, offline simulation analysis was performed using similar methodologies to those required to compute other interaxis coupling metrics in ADS-33E-PRF.
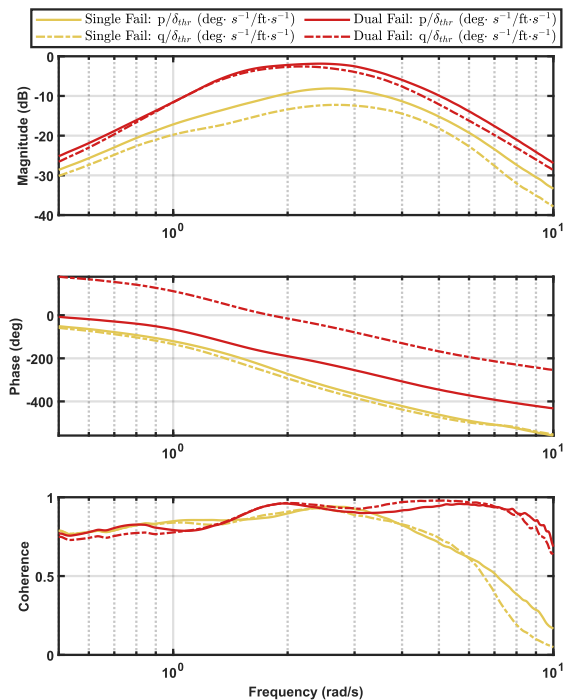
Figure 11. Roll and pitch due to heave frequency responses in ACAH mode.

Figure 11 shows roll and pitch rate due to heave frequency responses, which were generated from simulation of frequency sweep inputs in ACAH mode. The sweeps were injected at the pilot throttle input with an amplitude of ± 5 ft/s. This analysis mirrors that required to compute the roll-due-to-pitch and pitch-due-to-roll metrics for target tracking in ADS-33E-PRF. The magnitude of the off-axis coupling is largest near three rad/s, which is between the roll- and pitch-axis bandwidth and neutral stability frequencies, indicating potential handling qualities deficiencies. Additionally, the peak magnitude of the off axis coupling correlates to the frequency ranges of peak commanded torque in Figure 9. Similar results were found in TRC mode.

Figure 12 presents simulation data collected from vertical rate step commands in ACAH mode. The vehicle was trimmed at hover, then a step input was injected at the pilot throttle input. The maximum roll ($|\Delta\phi|_{max}$) and pitch ($|\Delta\theta|_{max}$) deviations within the first four seconds from the trim condition are plotted for the baseline, single motor failure, and dual motor failure cases. The maximum Euler angle deviations are nonlinear as a function of positive rate of climb (ROC) inputs due to nonlinear effects of torque saturation. The Euler angle displacements for negative ROC control inputs result in a linear relationship with $\dot{h}_{cmd}$ amplitude. Similar trends are seen in TRC mode. This analysis is comparable to the data collection methodology required to compute the yaw due to collective coupling metric in ADS-33E-PRF.
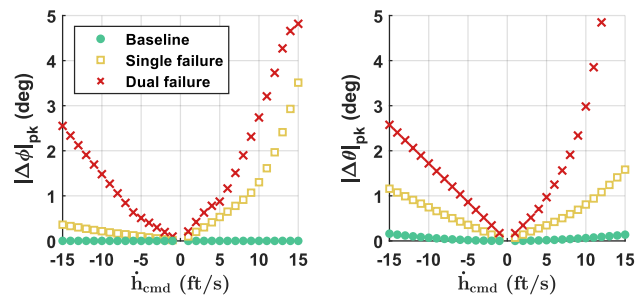
Figure 12. Maximum roll and pitch excursions due to vertical rate step inputs in ACAH mode.

Due to the potential for degraded handling qualities, these results, as well as the piloted simulation results to be discussed in a later section, indicate a clear need to develop predictive safety metrics that sufficiently characterize the roll and pitch response due to heave inputs during propulsion failures for UAM vehicles. The approaches presented herein serve as one example of this by mimicking the proven methods for characterizing other interaxis coupling responses outlined in ADS-33E-PRF. The time- and frequency-domain analysis both demonstrate potential handling qualities deficiencies due to this coupling. Future experiments are needed to develop predictive flying qualities metrics based on analyses such as these.

Roll and Pitch Coupling

Interaxis coupling between the roll and pitch axes were explored using frequency domain and time domain analysis. Frequency sweeps were applied to the roll and pitch pilot inputs for the baseline, single failure, and dual failure scenarios to assess the roll-due-to-pitch and pitch-due-to-roll metrics specified in ADS-33E-PRF. The off-axis frequency responses (q/δ_{lat} and p/δ_{lon}) were divided by the corresponding on-axis frequency responses (p/δ_{lat} and q/δ_{lon}) and averaged between the on-axis bandwidth and neutral stability frequencies. The results are plotted in Fig. 13 and show that the failures result in significant degradations in this metric. It is important to note that this metric uses the

11

frequency content between bandwidth and neutral stability frequencies of the on-axis response, which are usually representative of the 2-4 rad/s range. Pilot control strategies and tasks that result in lower input frequencies may not expose this deficiency. Analysis of the pilot control activity for a given task is needed to assess the validity of this metric for UAM vehicles.

Roll and pitch step responses of varying amplitude were applied to evaluate off axes Euler angle responses within the first four seconds following the control input. This metric is computed by dividing the maximum pitch ($\Delta\theta_{pk}$) and roll ($\Delta\phi_{pk}$) responses by the on-axis roll ($\Delta\phi_4$) and pitch angles ($\Delta\theta_4$) at four seconds. Figure 14 shows the ACAH pitch-due-to-roll ($\Delta\theta_{pk}/\Delta\phi_4$) versus the roll-due-to-pitch ($\Delta\phi_{pk}/\Delta\theta_4$) for step commands ranging from 6 to 26 degrees. The baseline cases remain near the origin, while the single and dual failure configurations experience increasing deviations with step command amplitude but remain within the Level 1 region. Figures 13 and 14 show that the frequency domain-based metric and time domain-based metric provide different handling qualities predictions for roll and pitch coupling.
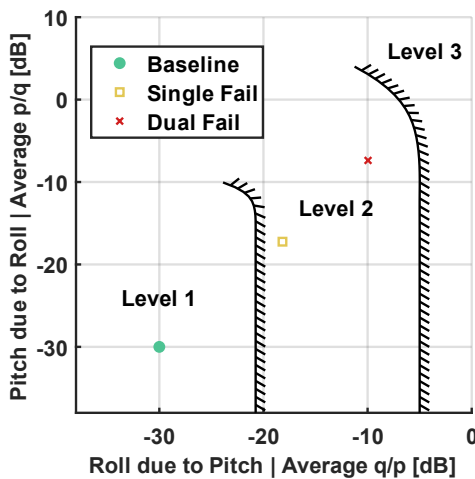
Figure 13. ADS-33E frequency domain-based pitch and roll interaxis coupling metric in ACAH.
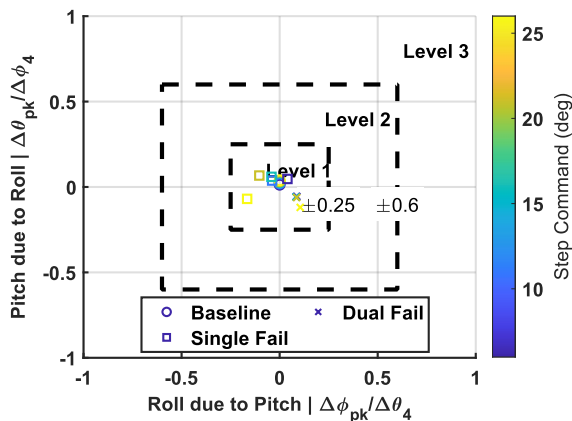
Figure 14. ADS-33E-PRF time domain-based pitch and roll interaxis coupling metric in ACAH.

EXPERMENTIAL SETUP

Simulation Facility

The handling qualities experiment was conducted in the Vertical Motion Simulator (VMS) at NASA Ames Research Center. The VMS provides a six degree-of-freedom (DOF) motion with 60 feet of vertical and 40 feet of lateral travel. The transport cab (T-cab) has dual pilot seats and seven-image presentation windows to provide outside imagery, as shown in Fig. 15.

Figure 15. NASA Ames VMS T-Cab cockpit interior.

The visual imagery was generated using an 8-channel RSi Image Generator which included a 72.07 millisecond delay with the projector. Figure 16 shows a pilot's front window view and an external view for the vertical maneuver task. The hover boards are shown as white squares and are used by the pilots to visually determine their position relative to the desired/adequate position boundaries.
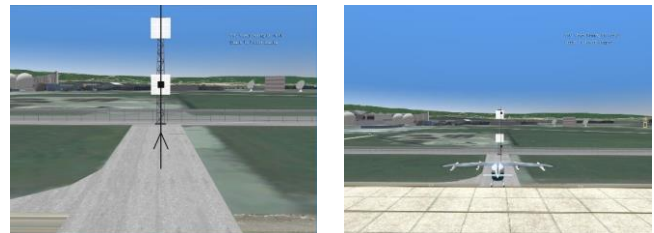
Figure 16. Pilot front view and external views for vertical maneuver. Hover boards are shown as white squares.

Aural cueing was provided to the pilot via a WaveTech sound generator and cab-mounted speakers. Rotor noise was emitted to mask the external noise from the VMS motion system and enhance the sense of immersion. The rotor noise was broadcast directionally as a function of airspeed, rotational speed, and thrust. Stopped rotors were modeled as silent.

The inceptor configuration included a right-hand side stick (RHSS), a left-hand thrust control lever (TCL), and pedals. The TCL and RHSS hand inceptors are shown in Figure 17. A switch on the RHSS is configured to allow the pilot to manually select the flight control mode between ACAH and TRC. The trim hat on the RHSS provides the pilot with pitch and roll trim capability in ACAH, and longitudinal and lateral translational rate trim in TRC. A switch next to the trim hat can be used to zero the trim inputs for those axes. The custom

TCL grip is configured at a 45° angle and operated in RCHH control mode for the entirety of the experiment. Pilots were able to set TCL friction settings during familiarization checkouts. The TCL trim hat was used for yaw trim only; trim inputs can be zeroed out using the TCL switch next to the trim hat.

A Primary Flight Display / Flight Director (PFD/FD) and Horizontal Situation Indicator (HSI) were electronically drawn on two 8-inch square flat panel displays at the right-hand cockpit station. Commanded and actual speed displayed on the PFD/FD and HSI automatically switch from airspeed (at or above 33.9 knots airspeed) to Ground Speed (below 33.9 knots airspeed).
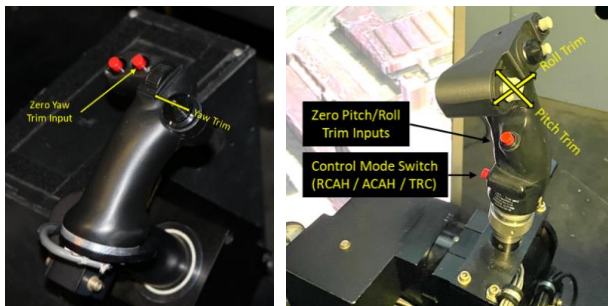
Figure 17. Thrust control lever (TCL) (left); Right-hand side stick (RHSS) (right).

Motor torque and voltage as a percentage (0-100%) of available limits are displayed for each motor on a panel-mounted multifunction display (MFD) located next to the primary flight instruments (Fig. 18). The MFD also displays RPM, temperature, and battery state of charge for each motor. For simplicity each rotor is assumed to be driven by a single motor and a dedicated battery pack. The pusher propeller and flaps were not used during this experiment. The color bars would turn red when saturation limits were reached. In the case of a single motor failure, the torque and voltage bars were empty.
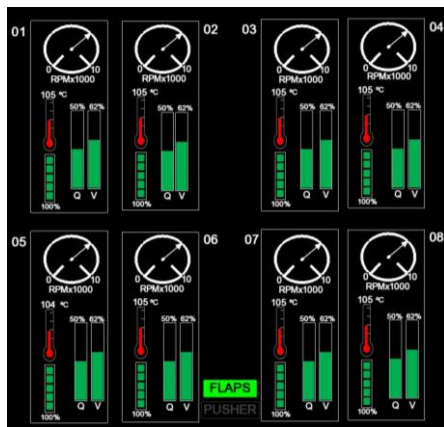
Figure 18: Multifunction Display (MFD)

The active control response mode was indicated to the pilot via illuminated momentary switches above the PFD. One of the switches was configured as a Master Caution alert. The Master Caution was annunciated in the event of a simulated powertrain failure, in conjunction with a cockpit warning tone. Pressing the Master Caution switch silenced the warning tone. The Master Caution light was red or orange while the response mode indicators are white or yellow.

Pilot Backgrounds

Six test pilots from the United States Army (U.S. Army), Federal Aviation Administration (FAA), and NASA participated in the handling qualities evaluation results presented in this paper. Pilot background information is shown in Table 9. All pilots were graduates from a test pilot school (TPS) program. Four of the pilots were predominantly of a rotorcraft background, while two pilots had a mixture of fixed and rotorcraft experience.

Table 9. Pilot background information.

Pilot	Organization	Primary Aircraft Experience
A	FAA	Fixed wing, rotorcraft
B	U.S. Army	Rotorcraft (CH-47)
C	FAA	Fixed wing
D	U.S. Army	Rotorcraft (AH-64)
G	NASA	Rotorcraft (V-22)
H	FAA	Rotorcraft

Vehicle-Task Configurations

Test configurations were evaluated using MTEs from ADS-33E-PRF and proposed HQTEs under evaluation by the FAA. The ADS-33E-PRF hover and low-speed MTEs are well established and proven handling qualities test evaluation standards for rotorcraft. The HQTEs are tailored versions of the MTEs designed to assess the operational challenges that will drive future acceptable certification standards for the UAM mission. Four tasks were selected to investigate the impact of propulsion failures on handling qualities and flight safety. The evaluations tasks, control mode, and participating pilots are shown in Table 10. This test matrix was repeated for baseline, single no torque failure, and dual low torque failure configurations. The performance criteria for the evaluation tasks are given in Tables 11, 12, and 13.

Table 10. Test matrix.

Task	Control Mode	Pilots
Vertical Maneuver MTE	ACAH and TRC	A,B,C,D
Vertical Reposition and Hold HQTE	ACAH and TRC	A,B,C,D
Lateral Reposition and Hold HQTE	ACAH and TRC	A,B,C,D
Hover MTE	ACAH and TRC	A,B,C,D, G*, H*

*Pilots G and H only evaluated ACAH configurations.

13

Table 11. Vertical Maneuver MTE and Vertical Reposition and Hold HQTE Performance Criteria/Method

Performance Criteria/ Method	ADS-33E	HQTE
Horizontal Position	±3/6 ft	±3/6 ft
Altitude	±3/6 ft	±3/6 ft
Heading	±5/10 deg	±5/10 deg
Completion time	13/18 s	24/29 s
Stabilize time	2 s	5 s
Delta altitude	25 ft	25 ft

Table 12. Lateral Reposition and Hold HQTE Performance Criteria/Method

Performance Criteria/Method	Value
Longitudinal Position	±5/10 ft
Altitude	±5/10 ft
Heading	±10/20 deg
Completion time	--
Ground Speed	10 ±2/4 kts
Maximum overshoot	5 ft
Maintain stable hover	5 s

Table 13. Hover MTE Performance Criteria/Method

Performance Criteria/Method	Value
Horizontal	±3/6 ft
Altitude	±2/4 ft
Heading	±5/10 deg
Timing	5/8 s
Maintain stable hover	30 s
Ground Speed	6-10 kts

Evaluation Procedure

At the start of each run, the aircraft was initialized in a hover with no failure present. The pilots were instructed to wait seven seconds before initiating the maneuver. If that run involved a propulsion failure, the motor failure(s) were triggered five to seven seconds following the start of the run. A master caution and warning tone were annunciated with the failure. Following the failure, the pilots silenced the warning tone, re-stabilized the aircraft, and returned close to the starting position. It was their discretion whether to trim the vehicle or hold nonzero RHSS inputs. Each evaluation session allowed for a limited number of practice runs per aircraft-task configuration, followed by at least three evaluation runs for the data record. The three evaluation runs formed the basis for the pilots' comments and HQRs using the Cooper-Harper

rating scale (Ref. 39). HQRs between 1-3 indicate that "adequate performance was attainable with a tolerable pilot workload" and was "satisfactory without improvement." HQRs between 4-6 indicate that "deficiencies warrant improvement" and HQRs between 7-9 indicate that "deficiencies require improvement." An HQR 10 indicates the vehicle was not controllable for the evaluated task and "improvement is mandatory".

PILOTED SIMULATION RESULTS

Vertical Maneuver

The HQRs for the vertical reposition and hold HQTE and the vertical maneuver MTE are given in Figs. 19 and 20 for the baseline, single motor fail, and dual low torque failure configurations. All pilots gave Level 1 ratings for the baseline configurations except for pilot C in ACAH mode.
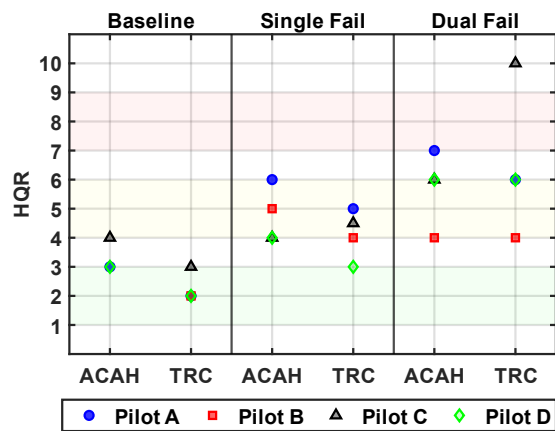
Figure 19. HQRs for vertical reposition and hold HQTE.
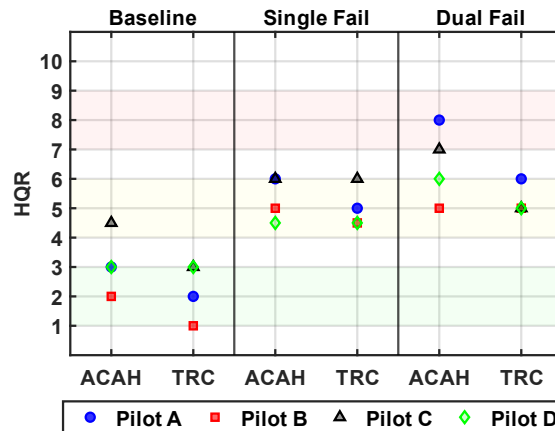
Figure 20. HQRs for vertical maneuver MTE.

Figure 21(a) shows the average maximum rate of climb (ROC) and motor torque percentage for the baseline evaluation runs. Pilot B did not evaluate the baseline configurations for ACAH for the vertical reposition and hold HQTE. The error bars represent the range of maximums across the three evaluation runs. The majority of the pilots' control strategy for the HQTE vertical maneuver started with an increase in TCL input to approximately 300-400 ft/min to

14

initiate the ascent (corresponding to approximately 60-70% of maximum torque), followed by a decrease in TCL input to capture the top hover board. This was followed by a negative TCL input (to approximately 20% torque) to initiate the descent. Figure 21(a) shows that pilot C had larger amplitude TCL inputs during ascent subphases in comparison to the other pilots, typically making TCL inputs that required above 80% of available torque which resulted in ROCs of approximately 500-600 ft/min. Higher magnitudes of vertical velocities may have caused difficulties making position captures and may have exposed heave response deficiencies that other pilots may not have experienced.
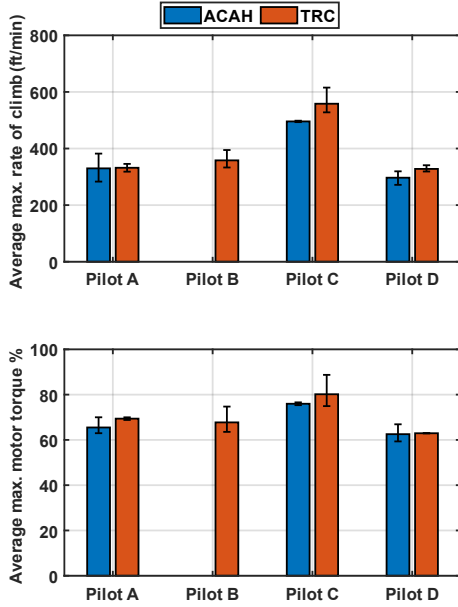
(a) Vertical reposition and hold HQTE (baseline)
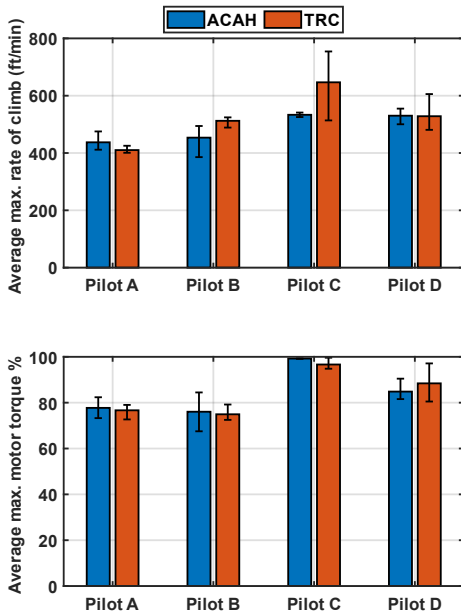
(b) Vertical maneuver MTE (baseline)

Figure 21. Maximum average ROC and motor torque percent during ascent phases.

Figure 21(b) shows the max ROC and motor torque percent for the ADS-33E-PRF vertical maneuver, which shows an increase in comparison to the HQTE maneuver. This suggests that the difference in timing requirements resulted in higher amplitude vertical rate commands. There were no pedal inputs required in any of the baseline evaluation runs. The majority of the pilots agreed that the bottom capture was the critical subphase of the task. The pilots noted throughout the evaluations that the lack of a detent on the TCL made it difficult to arrest the vertical velocity. The baseline HQRs improved in TRC mode which suggests that the higher augmentation decreased required pilot compensation by regulating translational velocities experienced during climbs and descents, allowing the pilots to direct their attention to the vertical axis.

The single and dual motor failures had a significant impact on task performance for both MTE and HQTE standards and control response types. This caused significant degradations in HQR and comments of PIO tendencies in the heave axis. The single motor failure resulted in almost all (but one) Level 2 HQRs, and the dual low torque failure resulted in a combination of Level 2 and Level 3 HQRs. The pilot control and compensation strategies were similar for each failure type. After recovering from the failure, the pilots re-stabilized the aircraft and returned close to the initial starting position. During the familiarization runs, the pilots noticed that large and abrupt TCL inputs commonly resulted in motor torque saturation and coupling in the pitch/roll axes. The aggressiveness metric, J_A, was used to compare TCL inputs between baseline and failure configurations. This metric is defined as

$$J_A = \frac{100\%}{T_r} \sum_{t=t_0}^{t_f} \frac{|\delta(t) - \delta_{trim}|}{\delta_{max} - \delta_{min}} \Delta t \qquad (15)$$

where $\delta(t)$ is a control input, T_r is the length of the recorded time interval, δ_{max} is the maximum control deflection, δ_{min} is the minimum control deflection, δ_{trim} is the trim control deflection and Δt is the time step. The aggressiveness metric was computed using the time interval ranging from the start of the task (t_0) to the end of the task (t_f). Discrete values for $\delta(t)$ were used which results in a summation rather than an integral. This metric has been used to characterize pilot workload for rotorcraft and fixed-wing configurations (Refs. 40-41). Figure 22 shows the TCL aggressiveness J_A for HQTE and ADS-33E-PRF versions of the vertical maneuver. Figure 22(b) shows a noticeable decrease in J_A.with the presence of propulsion failures relative to the baseline evaluation runs. Figure 22(a) shows a decrease in aggressiveness for most pilots, although pilot A increases aggressiveness for the single motor failure.

(a) Vertical reposition and hold HQTE

(b) Vertical maneuver MTE
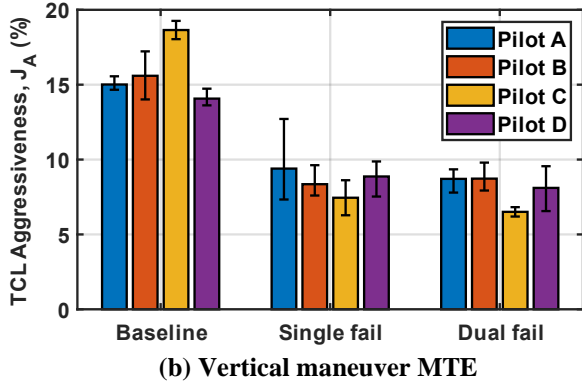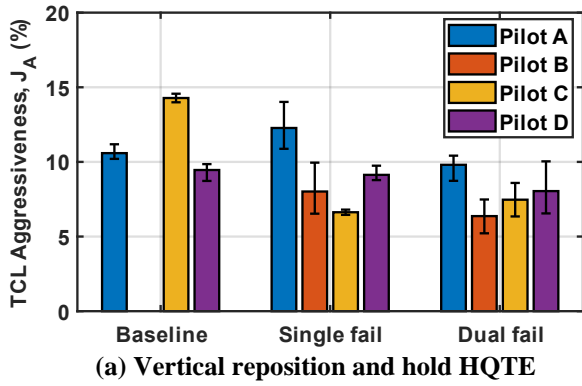
Figure 22. TCL aggressiveness metric in ACAH.

During the ascent/descent phases, roll and pitch due to heave resulted in undesired translational velocities which posed difficulties to maintain horizontal position. Figure 23 shows the vehicle lateral and longitudinal position throughout the task relative to the starting position (origin). The first evaluation run for the baseline and failure configurations are shown with the desired and adequate position boundaries. This shows that the presences of the propulsion failures often resulted in position excursions outside of the desired boundary and even exceeding the adequate boundary in some cases. Generally, the dual low torque failure resulted in larger position displacements than the single motor failure. The horizontal position error was larger in ACAH mode than in TRC mode.

The pilots commented that a tradeoff in degraded timing performance was required to avoid exciting the off-axis dynamics that could lead to over-control and instabilities. Figure 24 shows the pilot control activity for TCL and lateral/longitudinal inceptor inputs for each ACAH configuration. The control activity is characterized as the area under the power spectral density (PSD) estimate and is grouped into four frequency bands ranging from 0.2 to 10 rad/s. The area was averaged across the three evaluation runs. The first and second columns correspond to the RHSS and TCL control activities, respectively. Each row corresponds to a different pilot. The color bars represent baseline (no failure), single motor failure, and dual low torque failures. This figure shows that the magnitude of RHSS inputs increased significantly in the presence of failures. It also shows that the power of the TCL inputs decreased with the presence of the

failures, suggesting that the pilots reduced the amplitude of their inputs to avoid adverse effects of motor torque saturation.
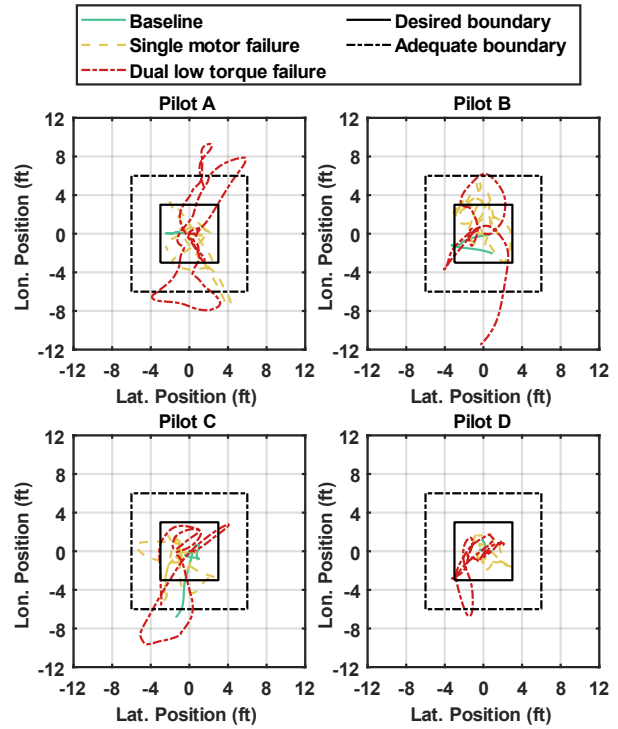
(a) ACAH
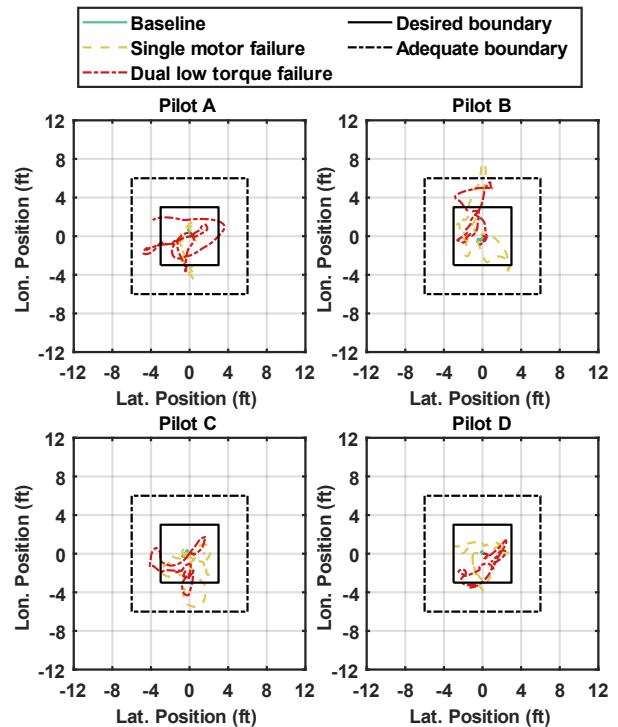
(b) TRC

Figure 23. Vehicle position for the vertical maneuver MTE.

16
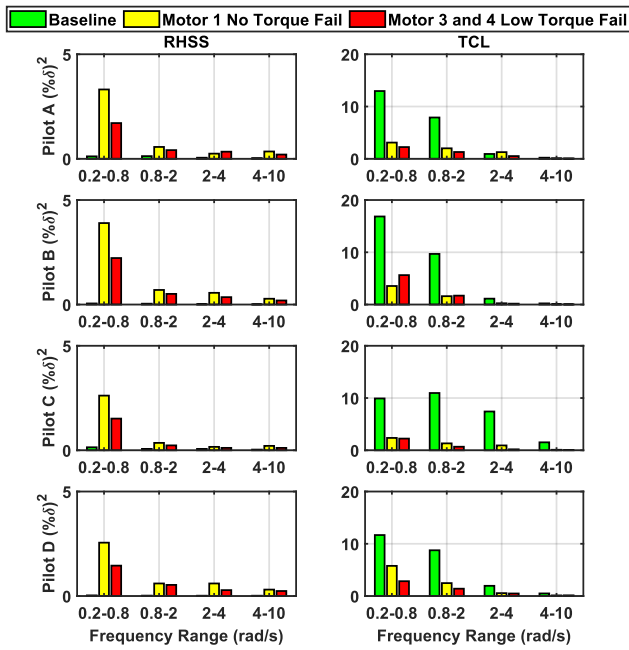
Figure 24. Pilot control activity for the vertical maneuver MTE in ACAH.
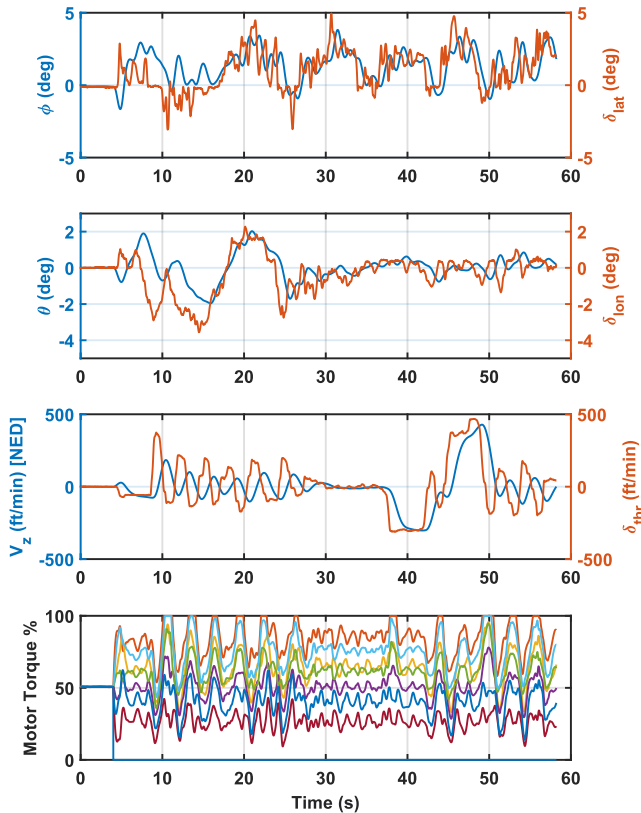
Figure 25. Vertical maneuver MTE, Pilot A, single motor failure, evaluation run 1, ACAH, HQR 6

The torque saturation often caused out of phase responses, which elicited comments of PIO tendencies in the heave and roll axes. Figure 25 shows a time history example for pilot

A's first evaluation run for the vertical maneuver in ACAH mode. The failure occurs at approximately five seconds following the start of the run. The pilot recovers from the failure and provides oscillatory and out of phase TCL inputs from eight to 30 seconds before getting out of the loop. The pilot initiates the maneuver at 37 seconds using +-5 ft/s vertical rate commands for the ascent/descent phases. The bottom capture subphase begins at approximately 50 seconds, resulting in out of phase TCL inputs again.

Overall, the primary contributing factors of the degradation in HQRs from failures were:

1. Cross coupling between heave and pitch/roll axes.

2. Pilot compensation to reduce amplitude and frequency of TCL inputs to avoid torque saturation.

3. Pilot compensation to provide RHSS inputs to maintain lateral/longitudinal position during ascent/descent phases.

4. Heave PIO tendency during bottom capture.

Lateral Reposition

Figure 26 shows the HQRs for the lateral reposition and hold HQTE for baseline, single motor no torque failure, and dual motor low torque failure scenarios.
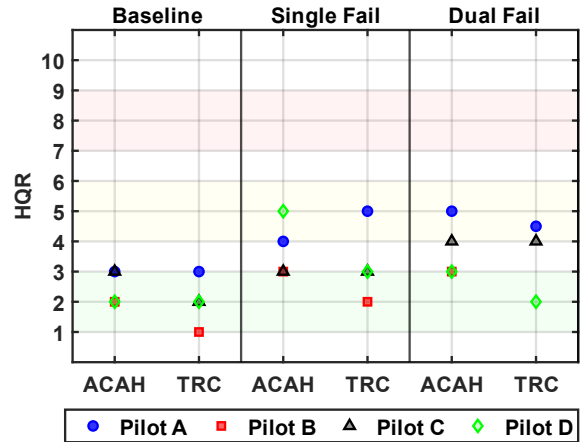
Figure 26. HQRs for lateral reposition and hold HQTE.

The baseline configuration was given Level 1 ratings from all pilots for both ACAH and TRC control modes. With no failures present, the pilots made primarily lateral RHSS inputs, and generally did not make TCL or pedal inputs. The critical subphases of the task were the deceleration and position capture. In ACAH, pilots commonly input 7–10-deg step bank angle commands to initiate the lateral acceleration up to approximately 8-12 knots. This bank angle was held until the pilot initiated the deceleration with a bank angle command in the opposing direction, often exceeding negative 10 deg (left wing down). In baseline TRC, the pilots made gradual ramp increases to 8-12 knots during the lateral translation. The RHSS was returned to detent, or slightly in

the opposing direction to execute the position capture. Multiple pilots commented on the "jerky" nature of the TRC response to abrupt inputs, making it difficult to make small amplitude corrections, and limited the achievable level of aggressiveness. The response is likely considered jerky because RHSS inputs in TRC result in body-axis angular rates to accelerate to the translational velocity setpoint. Whereas most conventional rotorcraft utilize cyclic control that allows tilt of the rotor thrust vector without abrupt changes in vehicle attitude. Although there were no Level 2 HQRs for the baseline TRC configuration, further investigation to improve TRC response characteristics for small and abrupt control inputs should be explored, particularly for improvements in ride quality. Overall, this task suggests that the baseline ACAH and TRC bandwidth and phase delays were suitable to consistently reach desired performance.

The propulsion failures had a varying impact on task performance, resulting in a combination of Level 1 and Level 2 ratings for both control modes. One aspect of the pilot compensation strategy was to avoid adverse effects of motor torque saturation by reducing lateral aggressiveness, as shown with the aggressiveness metric, J_A, applied to lateral RHSS inputs in Fig. 27. Pilot B did not evaluate the dual failure configuration in TRC. In both control modes, the pilots reduced their level of aggressiveness as characterized by this metric.

(a) ACAH

(b) TRC
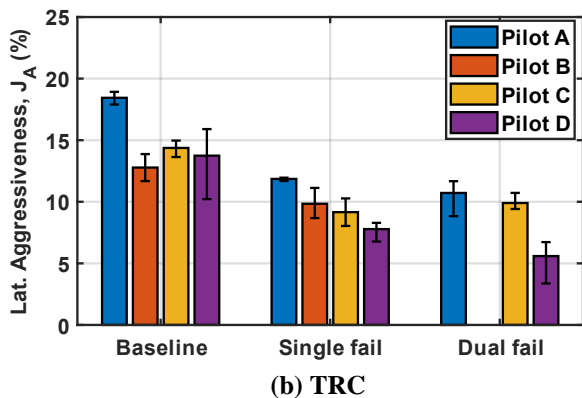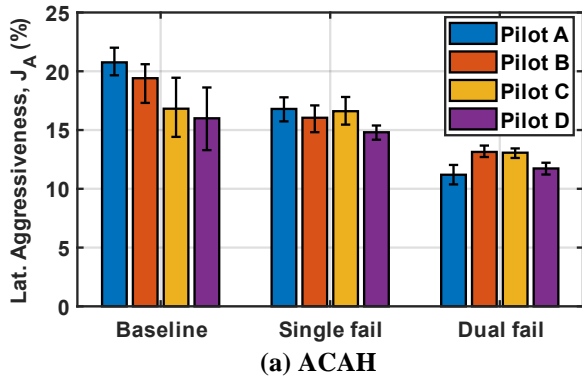
Figure 27. Lateral aggressiveness metric.

Figure 28 shows the vehicle's longitudinal and lateral position throughout the maneuver for the first evaluation of each control mode, baseline, and failure configuration. The baseline evaluation runs show that there were negligible

longitudinal displacements during the lateral translation subphase and small displacements (less than 5 feet) during the position capture subphase. The failures had the most impact on position keeping in ACAH control mode, primarily impacting the longitudinal position immediately following the failure, or at the final position capture point. On average, the position error was smaller in the TRC control mode, indicating the higher level of augmentation may have reduced pilot workload.
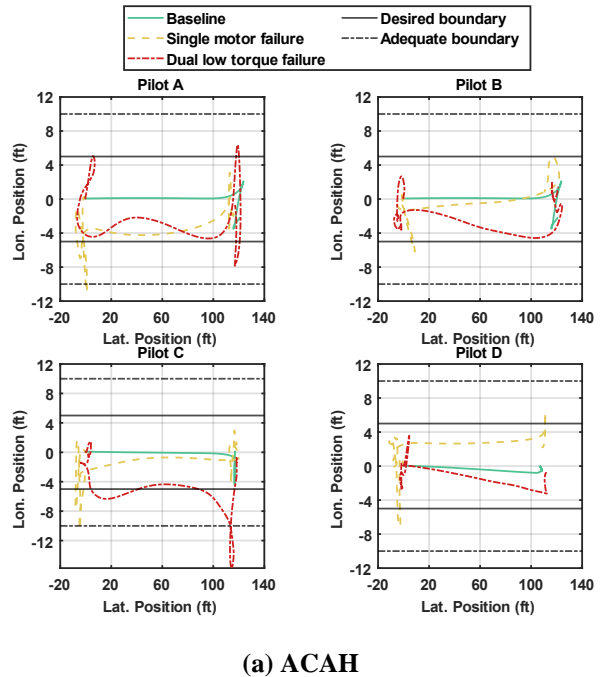
(a) ACAH
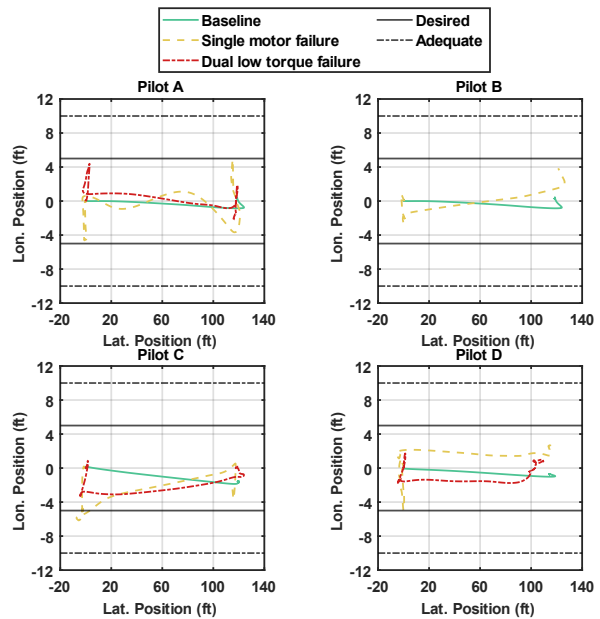
(b) TRC

Figure 28. Vehicle position throughout the lateral reposition and hold HQTE for baseline and failure configurations (evaluation run 1).

Increases in pilot control activity in the lateral and heave axis were typically correlated to degraded HQRs, particularly during the deceleration and capture subphase. Fig. 29 shows a time history of pilot C's first evaluation run with the dual low torque failure in ACAH. The start of the deceleration occurs at approximately 44 seconds with an abrupt control deflection to command a negative bank angle. This results in torque saturation, and out of phase characteristics in the lateral axis between 45 and 50 seconds. During this interval, there are also oscillatory body-axis roll rates between +-15 deg/s, and aft longitudinal position excursions slightly outside of adequate limits.
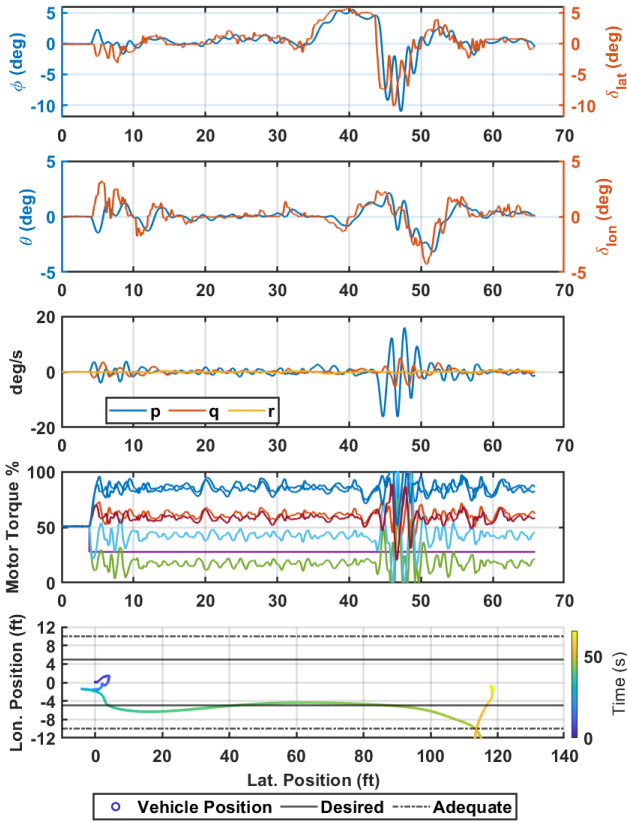
Figure 29. Lateral reposition HQTE, Pilot C, evaluation run 1, dual low torque failure, ACAH, HQR 4.

Figure 30 presents a scalogram of the corresponding evaluation run presented in Fig. 29 for the lateral, longitudinal and vertical rate pilot inputs. This shows the power of the pilot control inputs as a function of time for frequencies between 0.1 and 10 rad/s. The peak pilot control activity occurs within the first five seconds following the start of the deceleration subphase, which is designated with a vertical white line at approximately time=45 seconds. The lateral RHSS inputs and TCL inputs have peaks occurring at approximately 3 rad/s. These peaks correspond to the out of phase roll responses, torque saturation, and aft longitudinal drift shown in Fig. 29.
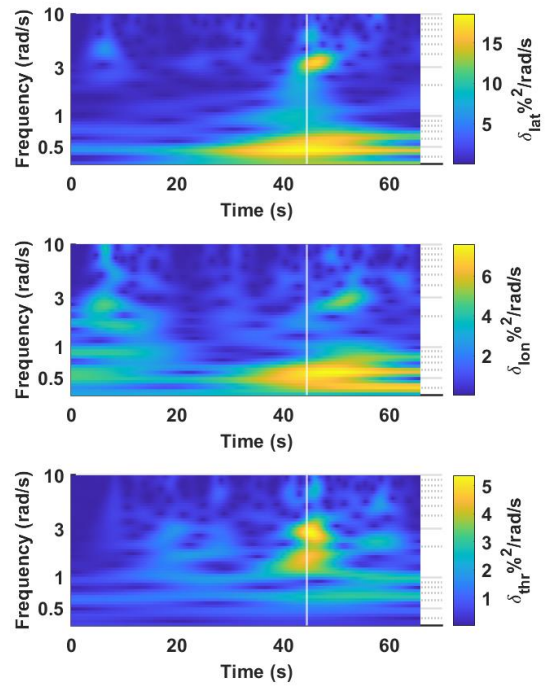
Figure 30. Scalogram for lateral reposition and hold HQTE, Pilot C, evaluation run 1, dual low torque failure, ACAH, HQR 4.
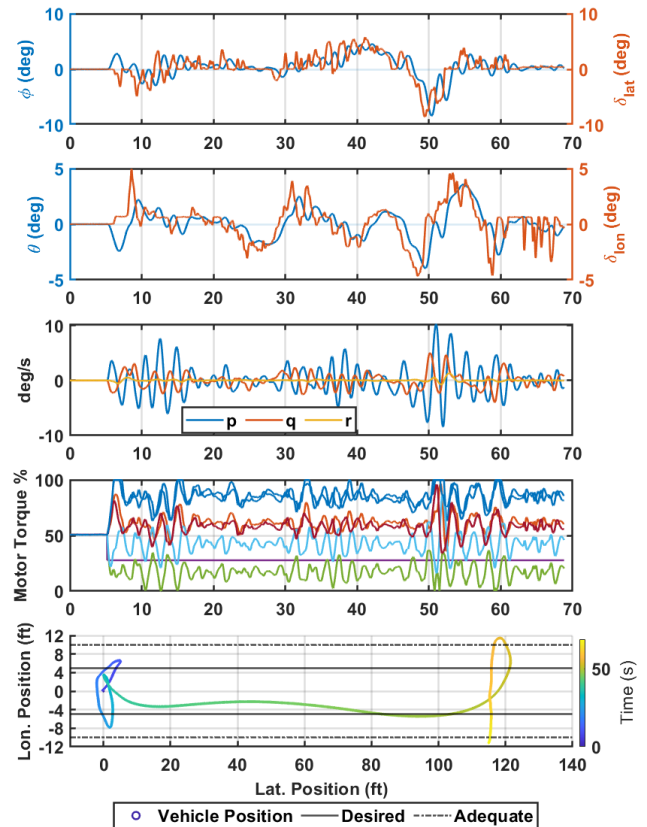
Figure 31. Lateral reposition HQTE, Pilot A, evaluation run 3, dual low torque failure, ACAH, HQR 5.

19
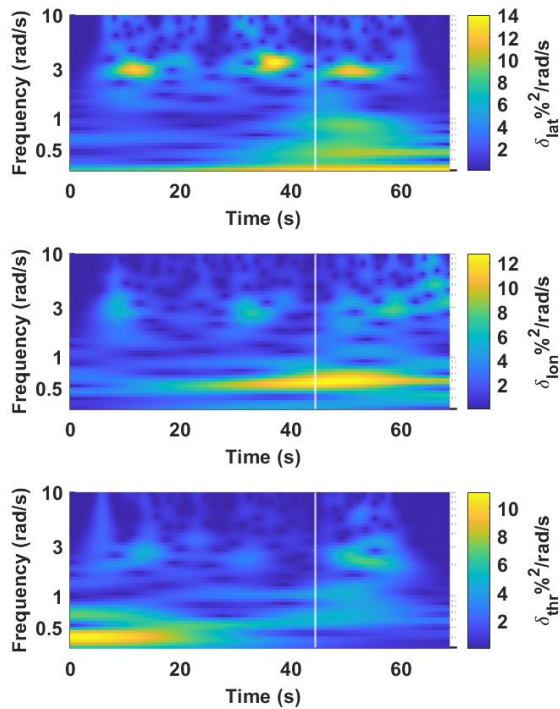
Figure 32. **Scalogram for lateral reposition and hold HQTE, Pilot A, evaluation run 3, dual low torque failure, ACAH, HQR 5.**

Figures 31 and 32 provide a similar example that illustrates the effects of increased control activity on degraded control system response and handling qualities characteristics. Figure 32 shows that the pilot is constantly making longitudinal inputs throughout the task to maintain longitudinal position. There were comments of oscillatory vehicle responses due to RHSS inputs, which is reflected by the oscillatory roll rate throughout the maneuver. Figure 32 shows that intervals of lateral RHSS and TCL inputs are near 3 rad/s at approximately 10s, 35s, and 50s. The peak TCL control activity occurs following the start of the deceleration phase and is correlated with longitudinal excursions slightly outside of adequate during the position capture.

Overall, the impact of the failures was dependent on the pilot control activity and level of aggressiveness. The primary causes of handling qualities degradations were:

1. Higher RHSS control activity during the deceleration subphase led to out of phase roll responses.

2. Vertical rate inputs with the TCL increased the motor torque commands, often resulting in torque saturation.

3. Pilot compensation in ACAH to provide longitudinal RHSS inputs during the lateral translation to avoid fore/aft drift.

4. Compensation to decrease RHSS aggressiveness to avoid hitting motor limits

Precision Hover

Figure 33 shows the HQRs for the hover MTE for each control mode and failure configuration. The baseline ACAH controller mostly resulted in Level 2 ratings. The primary reasons for the Level 2 ratings with ACAH were associated with difficulties timing the deceleration and capture, typically leading to overshoots with capture times exceeding desired performance. The majority of pilots had comments about unsatisfactory responses due to aggressive inputs and noted that they had to 'back off' for a smoother entry. The baselines TRC configuration showed improvements in comparison to the baseline ACAH. Pilots noted that there were very abrupt vehicle responses to sharp RHSS inputs, although they were able to use ramp inputs and to time the deceleration and capture phases. Three pilots gave the baseline TRC configuration a Level 1 rating, while Pilot C gave it a Level 2 rating with an HQR of 4. This could be a result of this pilot's increased activity on the pedal and throttle inputs, as all other pilots had negligible activity on these channels, instead letting the control system regulate the heading and altitude.
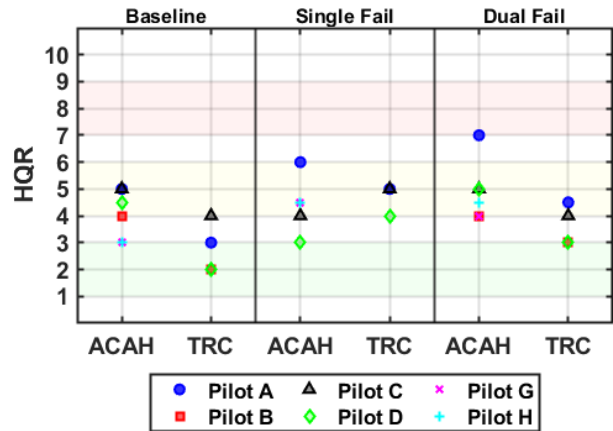
Figure 33. HQRs for the hover MTE.

The failure modes had different impacts on the pilot HQRs for the two control modes. In ACAH, the degradation in HQRs from the baseline to the failed configurations was minimal, likely due to the baseline Level 2 performance. In ACAH, the degradation of handling qualities due to the single failure is not clear, as some pilots gave better ratings for the single failure configuration than the baseline, while others did the opposite. For the dual failure, four pilots gave worse HQRs than for the baseline configuration, while two provided the same rating. However, in TRC, the median pilot ratings degrade from Level 1 to Level 2 for both failure modes.

Figure 34 shows the vehicle longitudinal and lateral position during the position capture and hold subphase of the task for a representative evaluation run for each failure configuration. Fig. 34(a) shows that, in ACAH mode, the position tracking

20

performance is comparable between the failed and non-failed configurations for all six pilots, with frequent deviations outside of the desired position boundary. In TRC, as shown in Fig. 34(b), the position excursions are much smaller and less frequent, and there is a noticeable degradation from the baseline configuration to the failed configurations. Desired performance was met for the baseline configuration for most runs, while a combination of desired and adequate performance was achieved for the failure cases. Typically, task performance was better for the dual low torque failure than the single no-torque failure, which is also reflected by the HQRs for TRC.
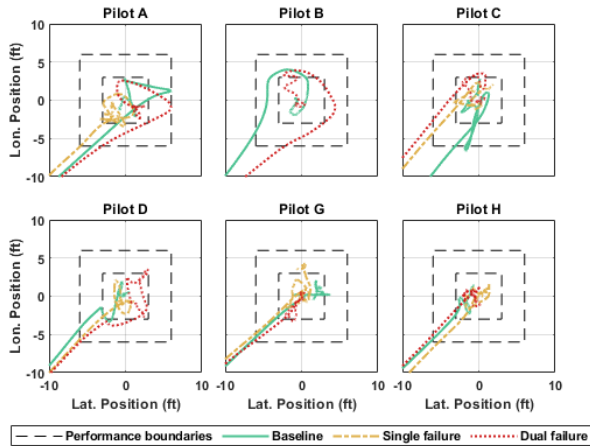
(a) ACAH
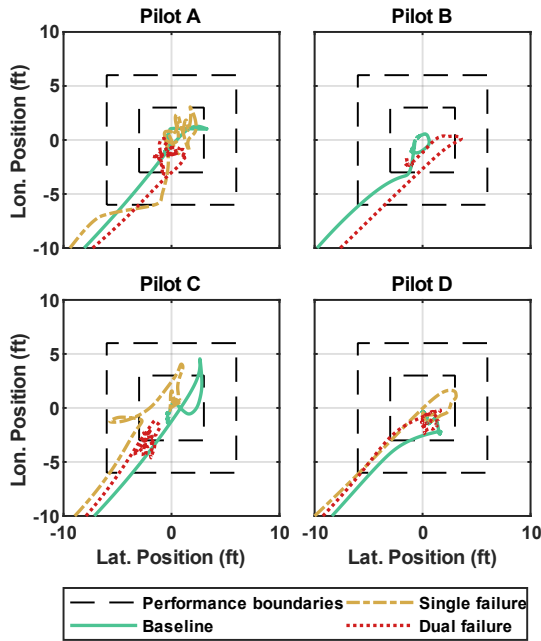
(b) TRC

Figure 34. Vehicle position during the capture and position hold subphase of the ADS-33E precision hover maneuver in (a) ACAH and (b) TRC modes.

Differences in pilot ratings for the same configuration often correlated with pilot input activity. In ACAH, the records with

the highest HQRs regularly showed increased throttle activity compared to others. An example of this is shown in Fig. 35, which shows an evaluation run from Pilot A of the dual failure configuration in ACAH, starting just prior to the deceleration into hover, which occurs at around 50 seconds. During the deceleration portion of the maneuver, the pilot observed motor saturation, which resulted in an unpredictable response and undesirable off-axis excursions, and comments on PIO tendencies in the heave axis. The motor torque time-history in the figure shows significant saturation from 57-73 seconds, which resulted in a heave response that was out-of-phase with the pilot's inputs.
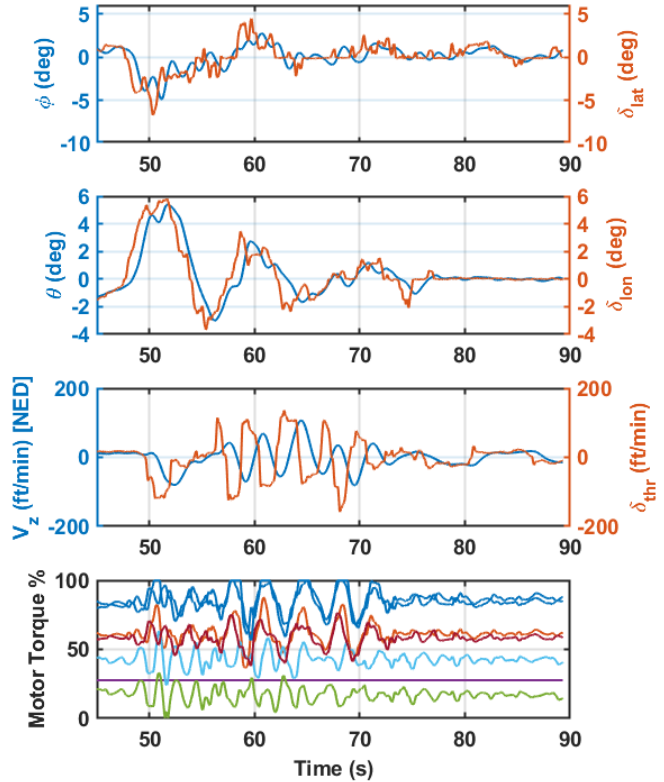
Figure 35. Hover MTE, Pilot A, evaluation run 3, dual low torque failure, ACAH, HQR 7.

In TRC, many pilots commented that learning and anticipating the right timing for the deceleration was a significant driver of HQRs. With the propulsion failures present, pilots often noted that they had to use smoother, smaller inputs to prevent inducing undesirable motion and ensure a smooth capture of the hover point, summed up by one pilot's comment that "less is more." In line with this, the evaluation run data shows a trend between pilot HQR and the root-mean-square (RMS) value of the RHSS inputs. This relationship is shown in Fig. 36. The data points represent the RMS values of the normalized lateral and longitudinal stick positions averaged across the pilots' evaluation runs and the HQR assigned for those runs. Larger RMS values correspond with lower HQRs, indicating that when pilots had to compensate and reduce their inputs, it resulted in a degraded rating. The Level 2 ratings with lower input RMS could be a

result of the pilots aiming for adequate performance rather than desired performance, which often resulted in larger overshoots and undesirable response characteristics.
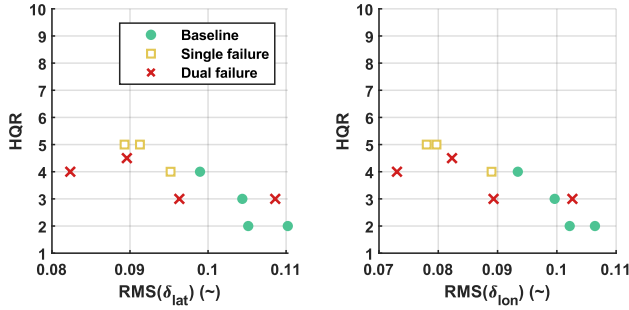
Figure 36. RHSS RMS values for hover MTE in TRC.

In summary, the impact of the failures on HQRs for the precision was minimal in ACAH but significant in TRC. The impact was dependent on the pilot control activity, aggressiveness, and compensation strategies. The primary causes of handling qualities degradations were:

1. Vertical rate inputs with the TCL induced undesirable off-axis motion and often resulted in torque saturation.

2. Compensation to decrease RHSS input magnitude to create a slower and more predictable deceleration into hover, which often resulted in adequate task performance with respect to the deceleration timing requirement.

CONCLUSIONS

A simulation-based study of the impact of propulsion failures on piloted handling qualities was completed. The objective of this work was to develop tools and metrics that may be used during conceptual design that specifically address safety of flight requirements.

Due to the complexities and nonlinear behaviors during failure scenarios, simulation modeling was a significant topic to be addressed. A nonlinear flight dynamics model was found to provide realistic impacts during failures which could impact the vehicle motions and pilot's responses to affect a desired recovery. The importance of modeling control saturation and PIO tendencies was a significant finding. Further work on including high crosswinds and turbulence is recommended.

Although modeling methods with increased complexity are continuing, an eventual goal is to consider the use and limitations of simpler linear models which would be implemented with conceptual design tools but capture the important dynamics characteristics. In addition, ongoing work on uncertainty quantification and sensitivity to control design will be an important part of providing feasible

modeling approaches especially where vehicle performance data may be limited.

The piloted simulation approach in a high-fidelity motion simulator was found to expose many important handling qualities issues during failures that could ultimately impact safety. This paper has presented an approach to providing realistic failure scenarios and focused solely on feasible propulsion failures. No attempt was made to identify the critical propulsion failure scenario, and this remains a topic for future research. In addition, other non-propulsion failures should be addressed. Use of the existing MTEs was found to provide a repeatable evaluation methodology and is recommended for future piloted simulation studies. However, the pilot ratings were found to be sensitive to performance parameters and maneuver criteria which should be considered for future studies. Lastly, handling qualities criteria included in existing specifications and other proposed criteria were found to be suitable for exposing handling qualities deficiencies. However, as described in previous sections, additional work on criteria not currently addressed is necessary and recommended.

The control law/system design approach was found to be an important influence on the results. While the intent of this study was to determine the degradation of handling qualities, as indicated by pilot ratings, the appropriate non-failed control design was important for determining this degradation. Also, the control type, such as ACAH and TRC, was found to produce different results in some cases. Since no attempt was made to consider failure-accommodating control strategies, further research is needed to determine the effect of automatic control systems that could detect and respond to failures and alleviating pilot workload and compensation such as that observed during the present test.

Several specific key conclusions can be drawn from the results presented in this research:

1. The vertical maneuver exhibited the most consistent and significant degradation in piloted handling qualities due to propulsion failures. These results correlated to predicted handling qualities levels using the interaxis coupling criteria in ADS-33E-PRF. Time history analysis and pilot comments indicated that undesired and excessive off-axis dynamics due to pilot inputs were the primary cause for the degradation.

2. Propulsion failures resulted in asymmetric rotor responses in a failed trim state using a nominal controller and control allocation. Some of the motors operated near control limits which often lead to saturation when pilots made TCL inputs.

3. The primary effects of the motor saturation were out of phase vehicle responses and interaxis coupling between the heave and pitch/roll axes. UAM eVTOL

vehicles will need a quantitative criterion to define allowable pitch and roll due to heave inputs.

Author contact: George Altamirano, george.altamirano@nasa.gov

ACKNOWLEDGMENTS

REFERENECS

1. Lawrence, B., Theodore, C.R., and Johnson, W., Berger, T., "A Handling Qualities Analysis Tool for Rotorcraft Conceptual Designs," *The Aeronautical Journal,* June 2018, Volume 122 No. 1252 960, pp 960–987

2. Altamirano, G.V., Foster, J.V., Malpica, C., and Schuet, S., "Integrated Handling Qualities Safety Analysis for Conceptual Design of Urban Air Mobility Vehicles," Proceedings of the AIAA AVIATION 2022 Forum, June 27-July 1, 2022, Chicago, IL & Virtual

3. Anon., "Handling Qualities Requirements for Military Rotorcraft," Aeronautical Design Standard-33 (ADS-33E-PRF), US Army Aviation and Missile Command, March 2000.

4. Klyde, D. H., Schulze, P. C., Mitchell, D. G., Sizoo, D., Schaller, R., and McGuire, R., "Mission Task Element Development Process: An Approach to FAA Handling Qualities Certification," Paper AIAA 2020-3285, AIAA AVIATION 2020 FORUM, June 15–19, 2020

5. Klyde, D., Jones, M., Shubert, M., Mitchell, D., Schaller, R., Sizoo, D., Webber, D., van Houdt, J., Feary, M., and Simmons, R., "Towards Handling Qualities and Automation Assessment for Certification of eVTOL Aircraft," Vertical Flight Society's 78th Annual Forum Proceedings, May 10–12, 2022

6. Mansur, M. H., and Schroeder, J. A., "An Investigation of the Ability to Recover from Transients Following Failures for Single-Pilot Rotorcraft," NASA TM 100078, May 1988.

7. Hindson, W. S., Eshow, M. M., and Schroeder, J. A., "A pilot rating scale for evaluating failure transients in electronic flight control systems," 17th Atmospheric Flight Mechanics Conference, Portland, OR August 20-22, 1990.

8. Weakley, J. M., Kleinhesselink, K. M., Mason, D. H. and Mitchell, D. G., "Simulation Evaluation of V-22 Degraded-Mode Flying Qualities," American Helicopter Society 59th Annual Forum, Phoenix, Arizona, May 6-8, 2003.

9. Mitchell, D. G. , Weakley, J. M., Kleinhesselink, K. M., and Mason, D. H., "Development of Mission Task Elements for V/STOLs," American Helicopter Society 59th Annual Forum, Phoenix, Arizona, May 6-8, 2003.

10. Mitchell, D. G., Mason, D. H., Weakley, J. M., and Kleinhesselink, K. M., "Piloted Evaluation of Degraded-Mode Handling Qualities," AIAA Atmospheric Flight Mechanics Conference and Exhibit, Providence, RI, August 16-19, 2004.

11. Blanken, C. L., Tischler, M. B., Lusardi, J. A., Berger, T., Ivler, C. M., and Lehmann, R., "Proposed Revisions to Aeronautical Design Standard – 33E (ADS-33E-PRF) Toward ADS-33F-PRF," Special Report SRFCDD-AMV-19-01, U.S. Army Combat Capabilities Development Command, September 2019.

12. Niemiec, R., Gandhi, F., Lopez, M. J. S., Tischler, M. B., "System Identification and Handling Qualities Predictions of an eVTOL Urban Air Mobility Aircraft Using Modern Flight Control Methods," VFS International 76th Annual Forum & Technology Display, Montréal, Québec, Canada, May 19–21, 2020.

13. Bahr, M., McKay, M., Niemiec, R., Gandhi, F., "Handling Qualities Assessment of Large Variable-RPM Multi-Rotor Aircraft for Urban Air Mobility," VFS International 76th Annual Forum & Technology Display, Virginia Beach, VA, October 6–8, 2020.

14. Withrow-Maser, S., Malpica, C., and Nagami, K., "Multirotor Configuration Trades Informed by Handling Qualities for Urban Air Mobility Application," Proceedings of the Vertical Flight Society's 76th Annual Forum & Technology Display, October 6–8, 2020.

15. Withrow–Maser, S., Malpica, C., Nagami, K., "Impact of Handling Qualities on Motor Sizing for Multirotor Aircraft with Urban Air Mobility Missions," Presented at the Vertical Flight Society's 77th Annual Forum & Technology Display, Virtual, May 10-14, 2021.

16. Malpica, C. and Withrow-Maser, S., "Handling Qualities Investigation of Variable Blade Pitch and Variable Rotor Speed Controlled eVTOL Quadrotor Concepts for Urban Air Mobility," Proceedings of the VFS International Powered Lift Conference 2020, January 21–23, 2020.

17. Withrow-Maser, S., Aires, J., Ruan, A., Malpica, C., and Schuet, S., "Evaluation of Heave Disturbance Rejection and Control Response Criteria on the Handling Qualities of Urban Air Mobility (UAM) eVTOL Quadrotors Using the Vertical Motion Simulator," Proceedings of the Vertical Flight Society's Aeromechanics for Advanced Vertical Flight Technical Meeting, January 25–27, 2022.

18. Aires, J., Withrow-Maser, S., Ruan, A., Malpica, C., and Schuet, S., "Analysis of Handling Qualities and Power Consumption for Urban Air Mobility (UAM) eVTOL Quadrotors with Degraded Heave Disturbance Rejection and Control Response," Proceedings of the Vertical Flight Society's 78th Annual Forum, May 10–12, 2022.

19. Jones, M., and Jusko, T., "Development and Testing of Scalable Mission Task Elements for Certification of eVTOL Aircraft," AIAA SciTech Forum, San Diego, CA, January 3-7, 2022.

20. Wechner, M., Marb, M. M., Zintl, M., Seiferth, D., and Holzapfel, F., "Design, Conduction and Evaluation of Piloted Simulation Mission Task Element Tests for Desired Behavior

Validation of an eVTOL Flight Control System," AIAA AVIATION Forum, Chicago, IL, June 27-July 1, 2022.

21. Silva, C., Johnson, W., Antcliff, K. R., and Patterson, M. D., "VTOL Urban Air Mobility Concept Vehicles for Technology Development," Paper AIAA 2018-3847, 2018 Aviation Technology, Integration, and Operations Conference, AIAA AVIATION Forum, Atlanta, GA, June 25–29, 2018.

22. Johnson, W., Silva, C., and Solis, E., "Concept Vehicles for VTOL Air Taxi Operations," Presented at the American Helicopter Society Technical Conference on Aeromechanics Design for Transformative Vertical Flight, San Francisco, CA, January 16–19, 2018.

23. Hirschberg, M., "Meet Cora: Kitty Hawk Unveils 2-Seat eVTOL," Vertiflite, 3, Vol. 64, AHS International, Fairfax, VA, 2018, pp. 44–46.

24. Swartz, K. I., "Charging Forward: New eVTOL Concepts Advance," Vertiflite, 4, Vol. 63, AHS International, Fairfax, VA, 2017, pp. 24–29.

25. Pitt, D. M., and Peters, D. A., "Theoretical Prediction of Dynamic-Inflow Derivatives," Vertica, Vol. 5, (1), 1883, pp. 21–34.

26. Johnson, W., "Rotorcraft Aeromechanics," Cambridge University Press, New York, 2013.

27. Krishnan, R., *Electric Motor Drives Modeling, Analysis, and Control*, Prentice Hall, Hoboken, New Jersey, 2001

28. Wait, J., and Jahns, T. M., "A new control technique for achieving wide constant power speed operation with an interior PM alternator machine," *In Industry Applications Conference*, Vol. 2, 2001, pp. 807-814.

29. Han, W., "Simulation Model Development of Electric Motor and Controller (Master's Thesis, Chalmers University of Technology, Gothenburg, Sweden)," 2017

30. Salyer, Z., "Thermal Models of Electric Powertrain Components for Cooling System Simulation and Design Requirements (Undergraduate Honors Thesis, The Ohio State University, Columbus, Ohio)," 2019.

31. Erdinc, O., Vural, B., and Uzunoglu, M., "A dynamic lithium-ion battery model considering the effects of temperature and capacity fading," IEEE 2009 International Conference on Clean Electrical Power, Capri, Italy, June 9-11, 2009.

32. Shabani, B., and Biju, M., "Theoretical Modelling Methods for Thermal Management of Batteries," *Energies*, Vol. 8, (9), 2015, pp. 10153-10177.

33. Johnson, W., "NDARC–NASA Design and Analysis of Rotorcraft," NASA/TP 2015-218751, National Aeronautics and Space Administration, April 2015.

34. Franklin, J. A., and Stortz, M. W., "Moving Base Simulation Evaluation of Translational Rate Command Systems for VSTOL Aircraft in Hover," TM-110399, NASA, June 1996.

35. Malpica, C. A., Theodore, C. R., Lawrence, B., and Blanken, C. L., "Handling Qualities of Large Rotorcraft in Hover and Low Speed," TP 2015–216656, NASA, March 2015.

36. Justin, C., Patel, S, Bouchard, E., Gladin, J., Verberne, J., Li, E., Ozcan, M., Rajaram, D., Mavris, D., D'Arpino, M., Aldemir, T., Rizzoni, G., Turkmen, G., Mayo, M., Bivens, C., "Reliability and Safety Assessment of Urban Air Mobility Concept Vehicles," CR-20210017385, NASA, March 2021.

37. Duda, H., "Prediction of Pilot-in-the-Loop Oscillations Due to Rate Saturation," Journal of Guidance, Control, and Dynamics, Vol. 20, (3), May–June 1997, pp. 581–587.

38. Jones, M., "The Use of the Open-Loop Onset Point (OLOP) to Predict Rotorcraft Pilot-Induced Oscillations," Proceedings of the 75th Annual Forum, May 13–16, 2019.

39. Cooper, G. E., and Harper, R. P., Jr., "The Use of Pilot Rating in the Evaluation of Aircraft Handling Qualities," NASA TND 5153, 1969.

40. Hanson, C., Schaefer, J., Burken, J., Larson, D., Johnson, M., "Complexity and Pilot Workload Metrics for the Evaluation of Adaptive Flight Controls on a Full Scale Piloted Aircraft," TM-2014-216640, NASA, February 2014.

41. Zheng, A, "Investigation of Bandwidth and Disturbance Rejection Properties of a Dynamic Inversion Control Law for Ship-Based Rotorcraft," Master's Thesis, Pennsylvania State University, December 2015.